Biophysical Journal
Article

Biophysical Society

Computational Lipidomics of the Neuronal Plasma Membrane

Helgi I. Ingólfsson,[1] Timothy S. Carpenter,[1] Harsh Bhatia,[2] Peer-Timo Bremer,[2] Siewert J. Marrink,[3] and Felice C. Lightstone[1,*]

[1]Biosciences and Biotechnology Division, Physical and Life Sciences Directorate; [2]Center for Applied Scientific Computing (CASC), Computational Directorate, Lawrence Livermore National Laboratory, Livermore, California; and [3]Groningen Biomolecular Science and Biotechnology Institute and the Zernike Institute for Advanced Materials, University of Groningen, Groningen, the Netherlands

ABSTRACT Membrane lipid composition varies greatly within submembrane compartments, different organelle membranes, and also between cells of different cell stage, cell and tissue types, and organisms. Environmental factors (such as diet) also influence membrane composition. The membrane lipid composition is tightly regulated by the cell, maintaining a homeostasis that, if disrupted, can impair cell function and lead to disease. This is especially pronounced in the brain, where defects in lipid regulation are linked to various neurological diseases. The tightly regulated diversity raises questions on how complex changes in composition affect overall bilayer properties, dynamics, and lipid organization of cellular membranes. Here, we utilize recent advances in computational power and molecular dynamics force fields to develop and test a realistically complex human brain plasma membrane (PM) lipid model and extend previous work on an idealized, "average" mammalian PM. The PMs showed both striking similarities, despite significantly different lipid composition, and interesting differences. The main differences in composition (higher cholesterol concentration and increased tail unsaturation in brain PM) appear to have opposite, yet complementary, influences on many bilayer properties. Both mixtures exhibit a range of dynamic lipid lateral inhomogeneities ("domains"). The domains can be small and transient or larger and more persistent and can correlate between the leaflets depending on lipid mixture, Brain or Average, as well as on the extent of bilayer undulations.

INTRODUCTION

Cellular membranes are complex assemblies of lipids and proteins that separate cellular compartments, as well as the cell interior from the outside environment. A typical plasma membrane (PM) contains hundreds of different lipid species that are actively regulated by the cell (1,2). The diverse set of lipids can regulate protein function through specific lipid-protein interactions and through general bilayer-protein interaction (i.e., changes in bilayer properties) (3–5). Additionally, lipids are non-uniformly distributed within the membrane plane (6,7) and are thought to reside close to a critical point (8), where large fluctuations in regions (domains) of locally increased/depleted lipid content are to be expected. The lipid segregation can further modulate membrane proteins, affecting local concentrations, aggregation, and trafficking (9,10). On one hand, lipid compositions vary significantly within a cell between the membranes of its different organelles and submembrane compartments (1,11–13), and between different cells, PM lipid composition differs by organism, cell stage, environmental factors, and cell and tissue types (14–18). On the other hand, altered lipid composition is linked to many diseases, e.g., cancers, HIV, diabetes, atherosclerosis, cardiovascular disease, and Alzheimer's disease (9,19,20).

The brain, in particular, appears to be especially susceptible to disease states that are enhanced or accelerated by lipid composition (21–23). For instance, specific phosphatidylinositolphosphate (PIP) lipids are involved in regulation of aspects of neuronal cell function, and PIP lipid imbalances have been linked to a number of major neurological diseases (23). Indeed, PIPs themselves can modulate ion flux through PM ion channels (24,25) by direct interaction with the ion channels or by modulating membrane charge. Moreover, these neuronal membrane lipids can influence both the function and localization of proteins within the PM of the neuron and, in effect, regulate synaptic throughput (22).

These lipid differences raise questions as to how complex changes in composition affect overall bilayer

Submitted August 11, 2017, and accepted for publication October 13, 2017.

*Correspondence: lightstone1@llnl.gov

Helgi I. Ingólfsson and Timothy S. Carpenter contributed equally to this work.

Editor: D. Peter Tieleman.

https://doi.org/10.1016/j.bpj.2017.10.017

properties, dynamics, and lipid organization of cellular membranes. Studying lipid structural heterogeneity is challenging because of the lack of experimental methods suitable for measuring nanoscale assemblies of soft bilayers and living cells in the required spatiotemporal resolution. Computational modeling has emerged as a powerful alternative method and has become indispensable for exploring dynamic biomembranes and lipids at the molecular level (26). The use of coarse-grained (CG) molecular dynamics simulations has increased the accessible length- and timescales (27) compared to all-atom simulations. At the CG resolution, a number of atoms are combined into functional groups, decreasing the number of particles in the system and smoothing the energy landscape. The smoother energy landscape allows for larger integration time steps and often leads to faster effective dynamics. CG methods neglect some of the atomistic degrees of freedom, losing accuracy, and are therefore not applicable to all problems. Currently at the CG resolution, multi-component membranes can be modeled that approach the complexity of realistic cell membranes (28–36).

Here, we developed a realistically complex model of a human "brain-like" PM and extend previous work on the idealized, "average" mammalian PM (28). Our results show both striking similarities and differences between the Brain and Average PM mixtures. Despite significant changes in lipid composition, the biggest contributors—increased cholesterol concentration and increased tail unsaturation in the brain—appear to act complementary to each other. The differences effectively influence the membrane in opposite directions, yet with similar magnitudes, leading to many overall bilayer properties being comparable. Both mixtures exhibit a range of lipid lateral in homogeneities, or domains. The domains are dynamic, and sizes fluctuate, and their size and correlation across the leaflets differ in the Average PM compared to the Brain and with the level of bilayer undulations.

MATERIALS AND METHODS

Neuronal PM composition

The Brain composition represents an idealized lipid composition of human brain tissue or, more specifically, a "typical" human neuronal PM mixture. Although several different membrane compositions exist for specific cells and cell regions within the brain (12–14), the relative dearth of available data made it more prudent to construct a model that possessed the general properties of membranes found within the brain. To capture a typical Brain PM composition, we derived a consensus from a number of studies that performed lipidomic measurements of neurons and brain tissue (37–49). Using the idealized mammalian PM mixture (28) as a reference, we adjusted percentages of lipid headgroup types and tail distributions based on the overall trends reported for brain tissue extractions and PM isolations that differed from the idealized mammalian PM (see Supporting Materials and Methods for details). An overview of the Brain and the Average compositions is given in Fig. 1, and the specific lipid types used, their ratio in the outer/inner leaflets, and the lipid counts in the simulations are listed in Table S1.

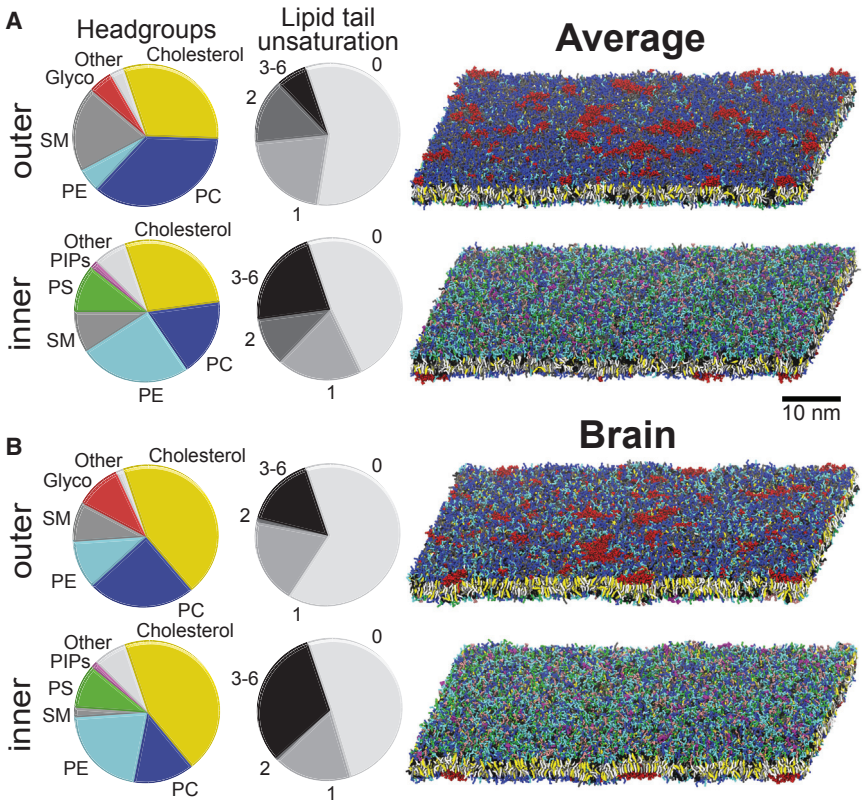

FIGURE 1 PM lipid distributions. Pie charts with the overall distribution of the main lipid headgroups and level of tail unsaturation in the outer/inner leaflet, as well as snapshots of the outer/inner leaflet of the simulations after 80 μs, are shown for the Average (*A*) and Brain membranes (*B*). The lipids in the snapshots are colored as follows: PC, *blue*; PE, *cyan*; SM, *gray*; PS, *green*; glycolipids (Glyco), *red*; PI, *pink*; PA, *white*; PIPs, *magenta*; CER, *ice blue*; Lyso, *orange*; DAG, *brown*; and cholesterol, *yellow*.

Force field

The simulations were performed using the Martini CG model (50,51). Most of the lipid force fields used were described in Ingólfsson et al. (28), including the PIP and ganglioside (GM) parameters, originally described in López et al. (52), and the improved cholesterol model (53). Control simulations using GMs with newly optimized clustering behavior (54) were also performed. Parameters for new Martini lipids were constructed according to the standard Martini 2.0 lipid building blocks and rules (50,51), as previously described (28,55). The details of the lipid force fields used are given in the Supporting Materials and Methods; all the lipid force fields, including the ones generated for this study, can be found at the Martini portal: http://www.cgmartini.nl.

Simulations

All the simulations were run using the GROMACS 4.6 simulation package (56), following the same setup described in Ingólfsson et al. (28). In short, a time step of 20 fs was used for all production runs with the standard Martini cutoffs, the same parameter set as denoted "common" in de Jong et al. (57). Each simulation contains ~20,000 lipids (or ~6000 for smaller control simulations) with >15 CG waters per lipid (one CG water representing four water molecules), counterions, and 150 mM NaCl; the exact lipid composition in each simulation is listed in Table S1. Membranes were constructed using the bilayer builder *insane* (55). For each bilayer mixture, the number of lipids in the inner/outer leaflet was adjusted based on an independent bilayer simulation with symmetrical composition of each leaflet (both leaflets being outer or inner). This process was iterated with changes in the cholesterol outer/inner leaflet distribution until the initial cholesterol distribution did not drift with time; i.e., the cholesterol distribution was allowed to adjust to its chemical potential in each leaflet, as detailed in the Supporting Materials and Methods and in Ingólfsson et al. (28). For the main simulations, large membrane undulations were restricted using weak position restraints on selected lipids in the outer leaflet (see Supporting Materials and Methods). Additional simulations with 10-fold weaker restraints and no restraints were also run. The temperature and pressure were controlled using the velocity rescaling thermostat (58) (at 310 K, with $\tau_T = 1.0$ ps) and the Parrinello-Rahman barostat (59) (1 bar semi-isotropic pressure, with $\tau_p = 5.0$ ps). Each membrane was simulated for 80 μs, corresponding to 320 μs of effective time, if accounting for the ~4-fold faster diffusion at the Martini CG level (51). All analysis was done either with respect to time or averaging over the last 2–10 μs of each simulation, as indicated. The analysis was carried out partly using tools provided in the GROMACS package and partly by custom tools written in Python and C++, to perform bilayer surface construction and topological analysis (60,61), as well as using the MDAnalysis package (62) and lipid-flow analysis methods (63), as described in the Supporting Materials and Methods.

RESULTS AND DISCUSSION

An idealized neuronal PM mixture was constructed (Brain; see Materials and Methods) and compared to the average mammalian PM mixture from Ingólfsson et al. (28) (Average). To compare the physical properties of the different PM lipid mixtures, large lipid patches (~20,000 lipids) of both lipid mixtures were simulated for 80 μs using the Martini CG force field (50,51) and their properties were analyzed. Note that bilayer undulations were suppressed in these systems to facilitate the analysis and to be representative of real membranes that are constrained by both the cytoskeletal network and the presence of membrane proteins.

Fig. 1 shows an overview of the main lipid headgroup and tail saturation distributions for both mixtures, as well as snapshots of the outer and inner leaflets after 80 μs. More detailed snapshots of the headgroups and tails are shown in Fig. S1 and a time-lapse sequence of the headgroups in Movie S1.

Global membrane properties; similar but different

Common properties of the two mixtures are listed in Table 1. Comparing the lipid composition of the two PM mixtures (Fig. 1 *A* and Table S1), the biggest differences are the significantly higher cholesterol content in the Brain, 44.5% compared to 30% in the Average PM, and the increased amount of polyunsaturated tails in Brain (on average, each lipid tail in the Brain has 1.27 double bonds compared to 1.05 in the Average PM). Because cholesterol is known to flip-flop between the leaflets within the time frame of the simulations, the cholesterol in both mixtures

TABLE 1 Membrane Properties

	Average		Brain	
	Outer	Inner	Outer	Inner
Average number of unsaturations per tail	0.77	1.32	0.90	1.63
Cholesterol fraction	0.54	0.46	0.51	0.49
Average area per lipid (nm^2)[a]	0.513	0.553	0.460	0.485
Average *sn*-1 tail order[b]	0.435	0.430	0.487	0.444
Average *sn*-2 tail order[b]	0.374	0.301	0.391	0.224
Average pos#3 tail order[b]	0.412	0.349	0.445	0.301
Average diffusion rates[c] (10^{-7} cm^2/s)	3.1 ± 0.3	4.3 ± 0.3	1.6 ± 0.2	2.8 ± 0.2
Average bilayer normal deviations[d]	13.07 ± 0.01		23.36 ± 0.09	
Bilayer thickness (nm)	4.109 ± 0.001		4.057 ± 0.002	
Flip-flop rates[e] (10^6 s^{-1})				
CHOL	7.290 ± 0.018		4.820 ± 0.004	
DAG	7.662 ± 0.049		2.800 ± 0.074	
CER	0.027 ± 0.006		0.015 ± 0.005	

[a]The average area per lipid (A_l) for the outer/inner leaflets was estimated in separate symmetrical simulations. SE values for A_l are ~0.001 nm^2.
[b]Lipid tail order was evaluated using the lipid tail order parameter (*S*). Flip-flopping lipids were excluded and averages weighted based on lipid counts in the respective leaflets. Either all bonds in the *sn*-1/*sn*-2 tails were averaged or the tail bond at position 3 was averaged between the tails. The weighted SE ~0.002. Tail order parameters for each lipid class are reported in Table S3.
[c]The weighted average of the lipid lateral diffusion coefficients (*D*) for all lipids that don't flip-flop. Note that lipid diffusion coefficients are reported as is, and no correction is applied for overestimates due to the larger effective simulation speed of CG simulations (51) or underestimates due to the periodically bound finite system sizes (79). All diffusion values are reported in Table S2.
[d]Average bilayer normal deviations are the average angle between the bilayer normal and the *z*-axis for each lipid (from the fitted bilayer surfaces) to the *z*-axes. Average over all lipids and the last 2 μs of the simulations (± SE, estimated using block averaging).
[e]Flip-flop rates (± SE) were measured as described in (28). For details on all calculated properties, see Supporting Materials and Methods.

was allowed to redistribute between the leaflets based on its chemical potential (see Supporting Material for details). In both mixtures, cholesterol preferentially localizes in the outer leaflet, but the emerging cholesterol asymmetry is much lower in the Brain (~1%) than in the Average PM (~5%). The bilayer average thickness (phosphate to phosphate distance) is comparable between the PMs (4.11 nm for the Average and 4.06 nm for the Brain, with SE <0.002). The density profiles along the box z-direction (Fig. 2) show similar peak locations. The Brain PM, despite having the same type of restraints on large-scale undulations, undulates more locally, leading to broader density distributions. Fitting the bilayer surfaces and measuring the average bilayer normal (all lipids over the last 2 μs) deviation from the z-axes, the Brain mixture deviates ~80% more than the Average mixture (Table 1). Additionally, the Brain PM has more cholesterol in the middle of the bilayer (Fig. 2), consistent with previous simulations and experiments showing higher preference for cholesterol in the bilayer center in more polyunsaturated bilayers (64). How much more depends somewhat on how you define being in the bilayer middle. Considering cholesterols within 0.8 nm of the bilayer center as in the middle, the Brain PM has 13% of the cholesterols in the middle compared to 7% in the Average, or ~75% more.

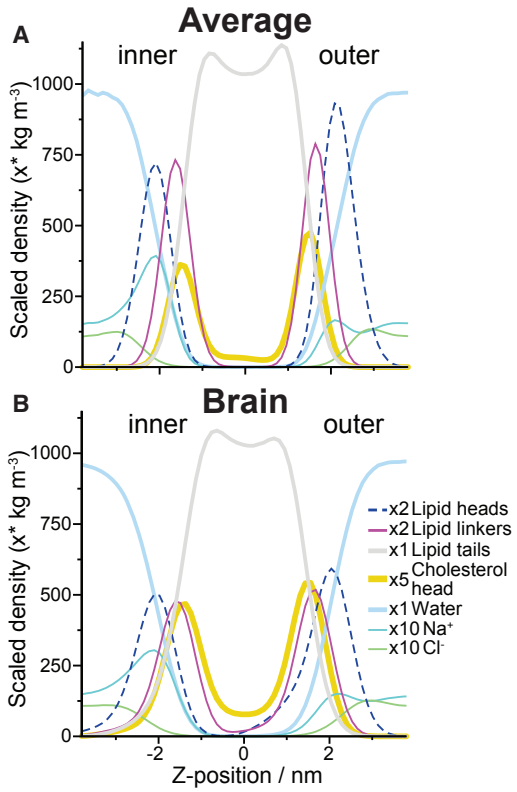

FIGURE 2 Membrane density profile. The density profile of the two different PM mixtures Average (*A*) and Brain (*B*) is shown across the Z-dimension, averaged from 78 to 80 μs. The Z-dimension is a reasonable approximation of the bilayer normal for these membranes as their undulations have been restricted. The density of the smaller groups is scaled for clarity, as indicated on the figure key.

Tail order was evaluated for all lipid types (Table S2). The tail order varies considerably due to their different headgroup and tail characteristics, but also based on the lipid location in the outer/inner leaflet or in the Average or Brain mixtures. In combination with the higher cholesterol content, the outer leaflets of both PMs contain lipids with somewhat longer and more saturated tails (Table S1), leading to higher tail order in the outer than in the inner leaflets (Table 1). For the Brain PM, the higher cholesterol content acts to increase the overall tail order, whereas the higher level of tail unsaturation acts to decrease the tail order. These two effects mostly balance out, with the overall tail order nearly the same in the Brain and the Average PMs (with an average tail order of 0.385 in the Average mixture and 0.386 in the Brain). However, if we look at the tail order in the outer and inner leaflets separately, there is a significant difference (Table 1). The Brain outer leaflet is more ordered than the Average outer leaflet, whereas the inner leaflet of the Brain is less ordered than the inner leaflet in the Average mixture. The increased tail order in the outer leaflet with respect to the inner leaflet is 11% for the Average and 31% for the Brain. Note that cholesterols influence the packing of other lipids but are not included in the tail order calculations themselves, as they do not contain fatty acid tails; cholesterol is mostly rigid, and given its significantly higher concentration in the Brain PM, the hydrocarbon core of the Brain PM is more "ordered" than that of the Average PM.

Lipid diffusion was also evaluated for each lipid type (Table S3). Just as with the tail order, lipid diffusion rates vary between the different lipid species, as well as their locations in the outer/inner leaflet and membrane type. Lipids in the more ordered outer leaflets diffuse slower than in the less ordered inner leaflets (Table 1), and the difference between the outer/inner leaflet diffusion rates is higher in the Brain than in the Average, in line with the larger difference in tail order. The overall lipid diffusion is ~40% slower in the Brain compared to the Average, even though the combined tail order is similar. This is presumably due to the higher cholesterol content in the Brain.

At the timescale of these simulations, cholesterol, diacylglycerol (DAG), and ceramide (CER) lipids flip-flop between the leaflets. The flip-flop rates are shown in Table 1, and similar to the lipid diffusion, lipid flip-flop is somewhat slower in the Brain. Previous simulation work showed a steep reduction in cholesterol flip-flop rate with increased cholesterol content and an increase in polyunsaturated bilayers (65). The effects of the ~15% increase in cholesterol content between the Brain and Average appear to be mostly compensated with an increase in the level of tail

unsaturation, resulting in only a modest reduction in flip-flop rates, ~35% for cholesterol.

Lipid mixing and domain sizes

In both the Average and the Brain PMs, the different lipid species are not homogeneously mixed in the bilayer plane. Based on their mutual interactions, lipids preferentially associate with other lipid species. At the ends of simulation (80 μs) snapshots (Figs. 1 and S1), glycolipid domains (*red*) can be seen in both PM mixtures; otherwise at that resolution, the mixture appears random. The snapshots of the lipid tails in Fig. S1 show preferential co-localization of polyunsaturated tails in both membranes, with more clusters of polyunsaturated tails in the Brain mixture, though of a somewhat smaller size. This is consistent with both mixtures having a significant fraction of polyunsaturated tails, but with more unsaturation in the Brain than the Average (Fig. 1; Table S1). In both mixtures, most of the polyunsaturated tails are on lipids where the other tail is saturated. The Brain mixture has a fraction where the other tail is monounsaturated (~5% of total lipids), but the Average mixture has a small fraction of lipids (~1.5% of total lipids) with both tails polyunsaturated.

To quantify preferential lipid-lipid interactions, we calculated the enrichment/depletion of the different lipid headgroups and linker types in their immediate neighborhood (defined as <1.5 nm) (Fig. S2). The lipid-lipid interaction profile for the Brain is very similar to the Average mixture, which is described in Ingólfsson et al. (28); the main features are domains of glycolipids in the outer leaflet and increased self-association of PIPs in the inner leaflet. The glycolipid domains can also be clearly seen by looking at the local lipid mobility or variations in the bilayer thickness (Fig. S3).

Cholesterol density is used to define bilayer domains that are enriched/depleted in cholesterol. Fig. 3 *A* shows the cholesterol density of the outer and inner leaflets of the last frame of the main Brain and Average PM simulations. Regions of high density (*red*) and low density (*blue*) are marked with contour lines (high density, *black lines*; low density, *white lines*). As the absolute cholesterol concentration varies between the PMs and their leaflets, we selected thresholds to define the high/low-density regions in each layer that maximize the number of domains in that layer (Fig. S4 *A*). Fig. S4 *B* shows the cumulative distribution function (CDF) of domain sizes with varying thresholds, demonstrating their sensitivity. Fig. 3 *B* shows domain size histograms of outer-leaflet high-density regions in the Brain and the Average mixtures. Histograms for the inner leaflets and low-density regions are shown in Fig. S4 *C*. Local cholesterol density fluctuates significantly in all layers. In main simulations (2 kJ mol^{-1} nm^{-2} undulation restraints), the Brain mixture has small and transient cholesterol domains and the Average mixture has larger, more persistent domains. Note that at this patch size

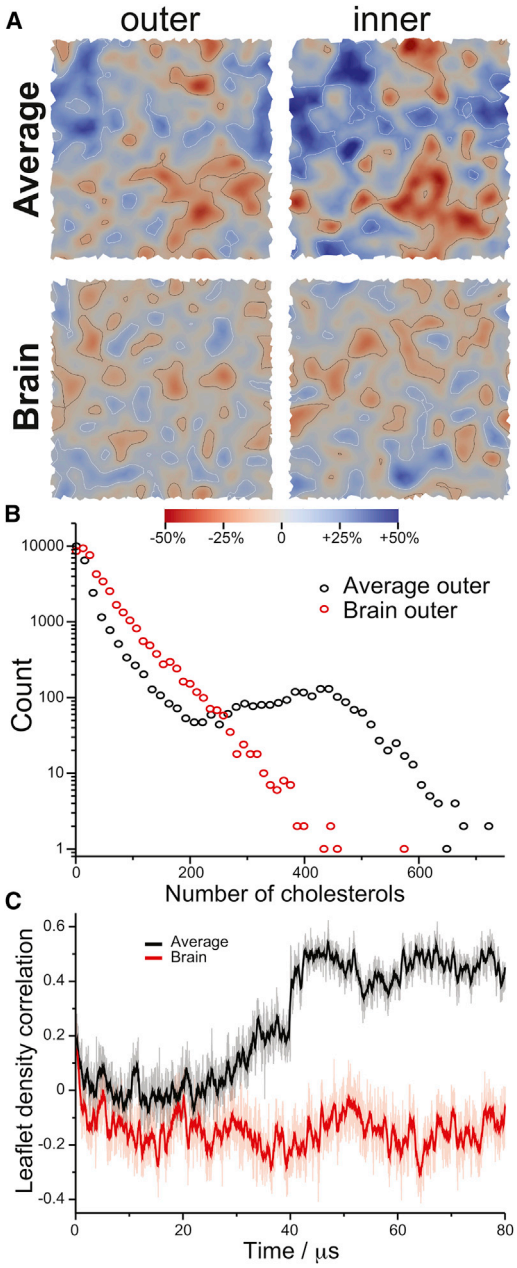

FIGURE 3 Lipid domains. In-plane lateral redistribution of cholesterol was used to track lipid patches of increased/decreased order for the outer/inner leaflets in both the Average and Brain mixtures. (*A*) Cholesterol density was mapped for each snapshot using a Gaussian filter and colored based on regions of increased (*red*) or decreased (*blue*) average density. Thresholds for high-density regions (*black contour lines*) and low-density regions (*white contour lines*) were determined as the values that maximized the number of domains in that layer (Fig. S4, *A* and *B*). (*B*) Histograms of domain "size," in number of cholesterols for the high-density regions of the outer leaflet; Fig. S4 *C* shows the same histograms for all other regions. (*C*) Cross correlation between the cholesterol densities of the PM's outer and inner leaflets, shown for every 5 ns (*dimmer lines*) and averaged over 500 ns (*bold lines*).

(~20,000 lipids), the buildup of larger domains in the Average mixtures takes tens of microseconds (Fig. S4 *D*). The size fluctuations are consistent with mixtures close to

a critical point (66,67), and the smaller domain sizes in the Brain mixture agree with the reduced phase separation observed with increased cholesterol content in giant PM vesicles (GPMVs) (68).

As seen in Fig. 3 *A*, the cholesterol density in the Average mixture is highly correlated between the leaflets, whereas the Brain mixture does not show such correlations. Fig. 3 *C* better depicts this, showing the cross correlation between the leaflets with time. In the Average mixture, the leaflet correlation builds up at about the same timescale as the larger domains form (Fig. S4 *D*), whereas in the Brain mixture, the leaflet correlation stays somewhat anti-correlated throughout the simulation. Averaging over the bilayer area and the last 10 μs of the simulations, the cross correlation is 0.45 ± 0.01 and -0.14 ± 0.01 in the Average and Brain mixtures, respectively. Numerous mechanisms have been proposed to drive leaflet coupling and domain registration, involving domain boundary line tension, inter-leaflet surface tension, cholesterol flip-flopping, bilayer undulation, local bilayer curvature, lipid curvature, and domain thickness mismatch (69–72). Any speculation in complex lipid mixtures like these, where the local domain composition varies and the boundaries are ill defined, is therefore troublesome; but notably, more local undulations are observed in the Brain mixture, where the asymmetry between leaflets (e.g., order, diffusion, tail unsaturation) is higher.

To analyze the lateral velocities of lipid regions, we used the lipid *Flows* methodology (63) (Fig. S5). As is to be expected, with both the Brain and Average mixtures, the regions of slower lateral lipid movement corresponded to the higher-cholesterol-concentration domains, whereas the faster-moving lipids were found in areas of lower cholesterol concentration. The overall rates of lipid lateral displacement (Fig. S5 *A*) were slower in the Brain mixture than in the Average mixture. Again, this is consistent with the fact that the Brain mixture contains significantly more cholesterol. Furthermore, when calculating the leaflet correlation function (the degree to which the lipid motions are correlated between the leaflets, see Supporting Materials and Methods), the Average mixture displays a very strong correlation between both leaflets (Fig. S5 *A*, *left images*). In contrast, the Brain mixture does not indicate a high correlation of lipid motions between the leaflets. This is in agreement with the previous cholesterol-density cross correlation. Interestingly, when the smoothing of the trajectory is averaged over a shorter temporal range (<20 ns), smaller pockets of correlated lipid regions become apparent for the Brain mixture (Fig. S5 *B*). These short-term correlated lipid motions reiterate the presence of small, transient cholesterol domains in the undulation-controlled Brain mixture.

Although bilayer undulations in cells are restricted due to the presence of the underlying cytoskeleton network as well as the high fraction of membrane proteins, it is of interest to study how bilayer undulations couple to the lipid organization and domain formation. As an initial exploration of the effects of undulations, additional simulations with either weaker or no restraints on undulations (0.2 and 0 kJ mol^{-1} nm^{-2} compared to 2 kJ mol^{-1} nm^{-2} in the main simulations) were performed. These simulations were started from the main Brain and Average PM simulations at 75 μs and simulated for 5 μs. Fig. 4 *A* shows a side view of the last frame of each simulation, demonstrating the undulation amplitude. We quantified the undulations by plotting the bilayer normal angle deviations with respect to the membrane normal, averaged over the entire membrane surface (Fig. 4 *B*). As expected, with weaker or no undulation restraints the bilayer undulations increase. At each level of restraint, the Brain mixture undulates more than the Average, pointing toward a lower bending modulus for the Brain membrane. Overall, the average bulk bilayer properties are similar for the different levels of undulations, e.g., the number of neighboring lipids showed no obvious deviation in the weaker and no-restraints simulations (see Fig. S2 for results on the main simulations and Fig. S6 *C* for the undulating case). All lipid neighbor enrichments/depletions changed by no more than 5%, i.e., no trends were observed with increasing curvature. The longer-scale lipid domain behavior, however, does change with different levels of undulations. Fig. 4 *C* shows the size histogram of cholesterol-enriched domains in the outer leaflet for the last 2 μs of each simulation (see Fig. S6 *B*) for results on different parts of the simulations. (Note that in Fig. 4 *C*, we plotted the cholesterol domain size and not the number of cholesterols as in Fig. 3 *B*. The shape of both curves is similar, compare Figs. 3 *B* and 4 *C*, *black and red curves*. Remarkably, with increased undulations, the domain sizes decrease in the Average mixture while they increase in the Brain. The reason for this behavior is unclear and requires more simulations at extended timescales to fully sample the coupling between domain sizes and undulatory modes. A clear coupling can be appreciated in the case of the glycolipids, which prefer regions of high negative curvature of the outer membrane leaflet (Fig. S6), consistent with previous simulation results (29). Notably, the bilayers tend to bend at glycolipid domain boundaries (Fig. S6 *A*), which may explain the growth of the cholesterol domains observed in the Brain membrane given the preferential co-localization of glycolipids and cholesterol (Fig. S2).

Additionally, after the Average PM model was published (28), a few small updates to Martini lipid parameters were made, as well as alternative parameters for the GM1 and GM3 lipids (54) (see Supporting Materials and Methods), and the effects of these changes were explored in smaller control simulations for both mixtures (Fig. S7). The average bilayer properties of the smaller alternative-parameter systems are very similar to those of the larger main simulations. The biggest difference is in the reduced ganglioside clustering using the recently modified version of the Martini GM1 and GM3 ganglioside lipid parameters, optimized

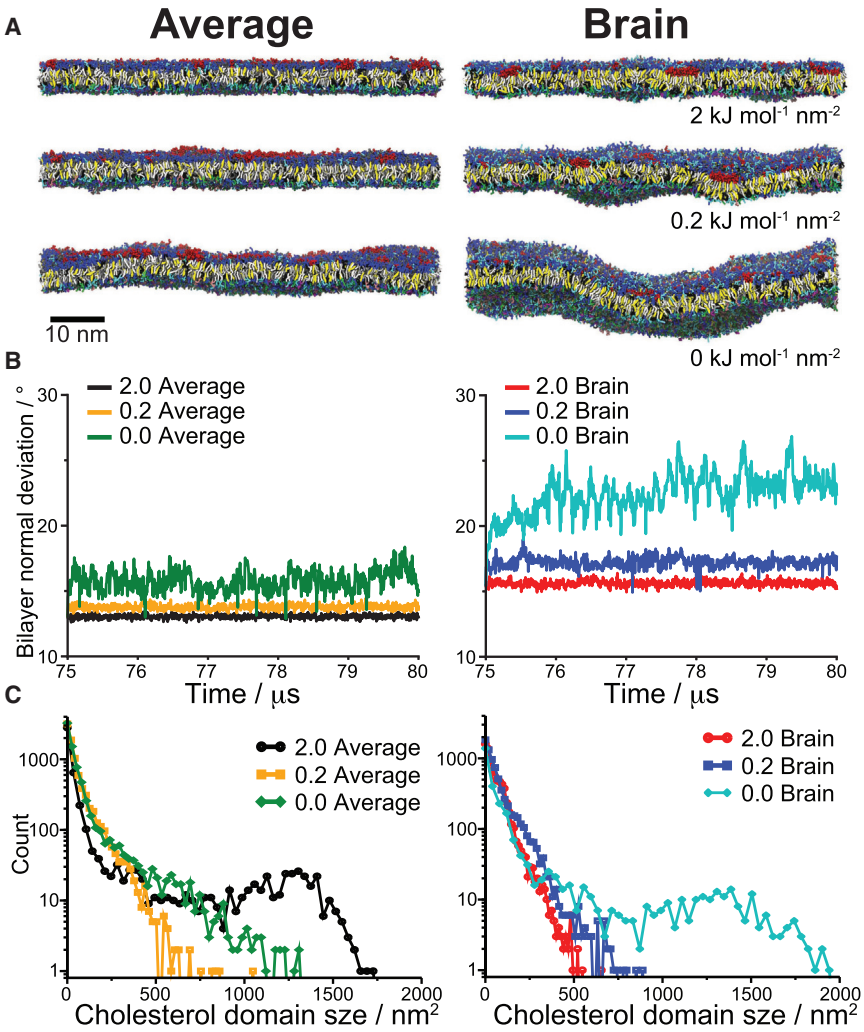

FIGURE 4 Effects of bilayer undulations. Starting from the main Brain and Average PM simulations at 75 μs, simulations with 10-fold weaker and no restraints on bilayer undulations (0.2 and 0 kJ mol^{-1} nm^{-2}, respectively) were run for 5 μs. (*A*) Side-view snapshots of the final structure of each simulation. The lipids are colored according to the same scheme as in Fig. 1. (*B*) The average bilayer undulations with time are shown as the average angle between the bilayer normal of each lipid (from the fitted bilayer surfaces) and the *z*-axis. (*C*) Size histograms of cholesterol-enriched domains in the outer leaflet of each simulation.

to better match the size of ganglioside clusters seen in atomistic simulations (54). As the smaller systems are not much larger than the largest cholesterol domains above, analyzing the cholesterol density using the same method was not very informative, but qualitative comparison of spatial two-dimensional cholesterol density maps averaged over the last 200 ns of the simulations (Fig. S7 *B*) show larger, more connected densities in Average PM than in the Brain at this undulation level (2 kJ mol^{-1} nm^{-2} restraints).

CONCLUSIONS

We assembled a realistically complex lipid model of a human neuronal PM (Brain), and despite significant differences in lipid composition (Fig. 1; Table S1), the overall bilayer properties show striking similarities to the recently published idealized mammalian plasma membrane (Average) (28). The higher cholesterol content of the Brain is balanced by more tail unsaturation, resulting in some average bilayer properties being comparable to those of the Average PM (see values for bilayer thickness and lipid tail order, diffusion, flip-flop, and average neighbors in Figs. 2 and S3; Tables 1, S2, and S3. Looking more closely, there are marked differences; the cholesterol asymmetry between the outer/inner leaflets is less pronounced in the Brain (Table 1), presumably due to saturation of preferred cholesterol lipid interactions; lipids in the Brain mixture diffuse and flip-flop more slowly (Tables 1 and S2), and the difference in properties between the outer and inner leaflets is greater in the Brain. Possible future work could involve exploring modulation of the cholesterol concentration or lipid tail unsaturation components independently.

Both mixtures are inhomogeneous and show significant fluctuation in local lipid concentrations. Defining domains as regions of high or low cholesterol density, we mapped the size and leaflet correlations of these domains. In the undulation-restrained simulations (2 kJ mol^{-1} nm^{-2} restraints), the Brain mixture has more cholesterol domains, but they are smaller and transient, whereas in the Average mixture, after considerable simulation time, larger persistent domains emerge (Figs. 3 and 4; Figs. S4 and S6). Interestingly, on the same timescale as the emergence of larger cholesterol

domains in the Average PM, the registration between the leaflets goes up, whereas in the Brain, the leaflets rapidly become somewhat anti-registered (Fig. 3; Fig. S5). However, the domain size distribution turned out to be very sensitive to the level of bilayer undulation (Fig. 4; Fig. S6). In particular, for the Brain membrane, high-amplitude undulatory modes are easily accessed, leading to coalescence of domains.

There are many interesting questions raised by the marked differences and similarities between the PMs. What is the acceptable range of changes in bilayer properties before cellular function is impaired? Are PM proteins such as ion channels and neuroreceptors sensitive to the presence of smaller, more transient, deregistered membrane domains? Is the only function of high cholesterol content in neurons to make the bilayers less permeable to ions, or are there additional benefits? Despite huge leaps forward in the fields of computational membrane studies, it is clear that in terms of understanding the full complexity and adaptability of cell-specific PMs, we have barely scratched the (highly complicated!) surface.

SUPPORTING MATERIAL

Supporting Materials and Methods, seven figures, three tables, and one movie are available at http://www.biophysj.org/biophysj/supplemental/S0006-3495(17)31132-3.

AUTHOR CONTRIBUTIONS

H.I.I., T.S.C., and F.C.L. designed the research. H.I.I. and T.S.C. performed the simulations. H.I.I., T.S.C., H.B., and P.T.B. performed the analysis; and all authors contributed to writing the paper.

ACKNOWLEDGMENTS

This work was partially funded by Laboratory Directed Research and Development at the Lawrence Livermore National Laboratory (16-FS-007). This work has been supported in part by the Joint Design of Advanced Computing Solutions for Cancer (JDACS4C) program established by the U.S. Department of Energy (DOE) and the National Cancer Institute (NCI) of the National Institutes of Health. We thank the Livermore Institutional Grand Challenge for the computing time. This work was performed under the auspices of the U.S. DOE by the Lawrence Livermore National Laboratory under contract DE-AC52-07NA27344, Los Alamos National Laboratory under contract DE-AC5206NA25396, Oak Ridge National Laboratory under contract DE-AC05-00OR22725, and Frederick National Laboratory for Cancer Research under contracts HHSN261200800001E. Release LLNL-JRNL-733434.

SUPPORTING CITATIONS

References (73–78) appear in the Supporting Material.

REFERENCES

1. van Meer, G., D. R. Voelker, and G. W. Feigenson. 2008. Membrane lipids: where they are and how they behave. *Nat. Rev. Mol. Cell Biol.* 9:112–124.
2. Sampaio, J. L., M. J. Gerl, …, A. Shevchenko. 2011. Membrane lipidome of an epithelial cell line. *Proc. Natl. Acad. Sci. USA.* 108:1903–1907.
3. Lee, A. G. 2004. How lipids affect the activities of integral membrane proteins. *Biochim. Biophys. Acta.* 1666:62–87.
4. Andersen, O. S., and R. E. Koeppe, II. 2007. Bilayer thickness and membrane protein function: an energetic perspective. *Annu. Rev. Biophys. Biomol. Struct.* 36:107–130.
5. Lundbaek, J. A., S. A. Collingwood, …, O. S. Andersen. 2010. Lipid bilayer regulation of membrane protein function: gramicidin channels as molecular force probes. *J. R. Soc. Interface.* 7:373–395.
6. Engelman, D. M. 2005. Membranes are more mosaic than fluid. *Nature.* 438:578–580.
7. Lingwood, D., and K. Simons. 2010. Lipid rafts as a membrane-organizing principle. *Science.* 327:46–50.
8. Veatch, S. L., P. Cicuta, …, B. Baird. 2008. Critical fluctuations in plasma membrane vesicles. *ACS Chem. Biol.* 3:287–293.
9. van Meer, G. 2005. Cellular lipidomics. *EMBO J.* 24:3159–3165.
10. Sezgin, E., I. Levental, …, C. Eggeling. 2017. The mystery of membrane organization: composition, regulation and roles of lipid rafts. *Nat. Rev. Mol. Cell Biol.* 18:361–374.
11. Klose, C., M. A. Surma, and K. Simons. 2013. Organellar lipidomics—background and perspectives. *Curr. Opin. Cell Biol.* 25:406–413.
12. O'Brien, J. S., and E. L. Sampson. 1965. Lipid composition of the normal human brain: gray matter, white matter, and myelin. *J. Lipid Res.* 6:537–544.
13. Kishimoto, Y., B. W. Agranoff, …, R. M. Burton. 1969. Comparison of the fatty acids of lipids of subcellular brain fractions. *J. Neurochem.* 16:397–404.
14. Breckenridge, W. C., G. Gombos, and I. G. Morgan. 1972. The lipid composition of adult rat brain synaptosomal plasma membranes. *Biochim. Biophys. Acta.* 266:695–707.
15. Christie, W. W. 1985. Rapid separation and quantification of lipid classes by high performance liquid chromatography and mass (light-scattering) detection. *J. Lipid Res.* 26:507–512.
16. Atilla-Gokcumen, G. E., E. Muro, …, U. S. Eggert. 2014. Dividing cells regulate their lipid composition and localization. *Cell.* 156:428–439.
17. Levental, K. R., J. H. Lorent, …, I. Levental. 2016. Polyunsaturated lipids regulate membrane domain stability by tuning membrane order. *Biophys. J.* 110:1800–1810.
18. Tulodziecka, K., B. B. Diaz-Rohrer, …, I. Levental. 2016. Remodeling of the postsynaptic plasma membrane during neural development. *Mol. Biol. Cell.* 27:3480–3489.
19. Fernandez, C., M. Sandin, …, O. Melander. 2013. Plasma lipid composition and risk of developing cardiovascular disease. *PLoS One.* 8:e71846.
20. Holthuis, J. C. M., and A. K. Menon. 2014. Lipid landscapes and pipelines in membrane homeostasis. *Nature.* 510:48–57.
21. Mattson, M. P., and T. Magnus. 2006. Ageing and neuronal vulnerability. *Nat. Rev. Neurosci.* 7:278–294.
22. Müller, C. P., M. Reichel, …, J. Kornhuber. 2015. Brain membrane lipids in major depression and anxiety disorders. *Biochim. Biophys. Acta.* 1851:1052–1065.
23. Waugh, M. G. 2015. PIPs in neurological diseases. *Biochim. Biophys. Acta.* 1851:1066–1082.
24. Zhou, P., H. Yu, …, M. Li. 2013. Phosphatidylinositol 4,5-bisphosphate alters pharmacological selectivity for epilepsy-causing KCNQ potassium channels. *Proc. Natl. Acad. Sci. USA.* 110:8726–8731.
25. Takahashi, N., S. Hamada-Nakahara, …, S. Suetsugu. 2014. TRPV4 channel activity is modulated by direct interaction of the ankyrin domain to $PI(4,5)P_2$. *Nat. Commun.* 5:4994.
26. Ingólfsson, H. I., C. Arnarez, …, S. J. Marrink. 2016. Computational 'microscopy' of cellular membranes. *J. Cell Sci.* 129:257–268.

27. Ingólfsson, H. I., C. A. Lopez, …, S. J. Marrink. 2014. The power of coarse graining in biomolecular simulations. *Wiley Interdiscip. Rev. Comput. Mol. Sci.* 4:225–248.
28. Ingólfsson, H. I., M. N. Melo, …, S. J. Marrink. 2014. Lipid organization of the plasma membrane. *J. Am. Chem. Soc.* 136:14554–14559.
29. Koldsø, H., D. Shorthouse, …, M. S. P. Sansom. 2014. Lipid clustering correlates with membrane curvature as revealed by molecular simulations of complex lipid bilayers. *PLOS Comput. Biol.* 10:e1003911.
30. Koldsø, H., T. Reddy, …, M. S. P. Sansom. 2016. Membrane compartmentalization reducing the mobility of lipids and proteins within a model plasma membrane. *J. Phys. Chem. B.* 120:8873–8881.
31. Reddy, T., and M. S. P. Sansom. 2016. The role of the membrane in the structure and biophysical robustness of the dengue virion envelope. *Structure.* 24:375–382.
32. Arnarez, C., S. J. Marrink, and X. Periole. 2016. Molecular mechanism of cardiolipin-mediated assembly of respiratory chain supercomplexes. *Chem. Sci.* (*Camb.*). 7:4435–4443.
33. Holdbrook, D. A., R. G. Huber, …, S. Khalid. 2016. Dynamics of crowded vesicles: local and global responses to membrane composition. *PLoS One.* 11:e0156963.
34. Marino, K. A., D. Prada-Gracia, …, M. Filizola. 2016. Impact of lipid composition and receptor conformation on the spatio-temporal organization of μ-opioid receptors in a multi-component plasma membrane model. *PLOS Comput. Biol.* 12:e1005240.
35. Jeon, J.-H., M. Javanainen, …, I. Vattulainen. 2016. Protein crowding in lipid bilayers gives rise to non-gaussian anomalous lateral diffusion of phospholipids and proteins. *Phys. Rev. X.* 6:021006–021017.
36. van Eerden, F. J., T. van den Berg, …, S. J. Marrink. 2017. Molecular dynamics of photosystem II embedded in the thylakoid membrane. *J. Phys. Chem. B.* 121:3237–3249.
37. Wells, M. A., and J. C. Dittmer. 1967. A comprehensive study of the postnatal changes in the concentration of the lipids of developing rat brain. *Biochemistry.* 6:3169–3175.
38. Lutzke, B. S., and J. M. Braughler. 1990. An improved method for the identification and quantitation of biological lipids by HPLC using laser light-scattering detection. *J. Lipid Res.* 31:2127–2130.
39. Kracun, I., H. Rosner, …, G. Lauc. 1991. Human brain gangliosides in development, aging and disease. *Int. J. Dev. Biol.* 35:289–295.
40. Diagne, A., J. Fauvel, …, L. Douste-Blazy. 1984. Studies on ether phospholipids. II. Comparative composition of various tissues from human, rat and guinea pig. *Biochim. Biophys. Acta.* 793:221–231.
41. Homan, R., and M. K. Anderson. 1998. Rapid separation and quantitation of combined neutral and polar lipid classes by high-performance liquid chromatography and evaporative light-scattering mass detection. *J. Chromatogr. B Biomed. Sci. Appl.* 708:21–26.
42. Han, X., D. M. Holtzman, and D. W. McKeel, Jr. 2001. Plasmalogen deficiency in early Alzheimer's disease subjects and in animal models: molecular characterization using electrospray ionization mass spectrometry. *J. Neurochem.* 77:1168–1180.
43. Han, X., and R. W. Gross. 2005. Shotgun lipidomics: electrospray ionization mass spectrometric analysis and quantitation of cellular lipidomes directly from crude extracts of biological samples. *Mass Spectrom. Rev.* 24:367–412.
44. Sharon, R., I. Bar-Joseph, …, D. J. Selkoe. 2003. Altered fatty acid composition of dopaminergic neurons expressing α-synuclein and human brains with α-synucleinopathies. *J. Biol. Chem.* 278:49874–49881.
45. Chan, R. B., T. G. Oliveira, …, G. Di Paolo. 2012. Comparative lipidomic analysis of mouse and human brain with Alzheimer disease. *J. Biol. Chem.* 287:2678–2688.
46. Abbott, S. K., P. L. Else, T. A. Atkins, and A. J. Hulbert. 2012. Fatty acid composition of membrane bilayers: importance of diet polyunsaturated fat balance. *Biochim. Biophys. Acta.* 1818:1309–1317.
47. Lam, S. M., Y. Wang, …, G. Shui. 2014. Brain lipidomes of subcortical ischemic vascular dementia and mixed dementia. *Neurobiol. Aging.* 35:2369–2381.
48. Arai, Y., J. L. Sampaio, …, W. B. Huttner. 2015. Lipidome of midbody released from neural stem and progenitor cells during mammalian cortical neurogenesis. *Front. Cell. Neurosci.* 9:325.
49. Oliveira, T. G., R. B. Chan, …, N. Sousa. 2016. The impact of chronic stress on the rat brain lipidome. *Mol. Psychiatry.* 21:80–88.
50. Marrink, S. J., A. H. De Vries, and A. E. Mark. 2004. Coarse grained model for semiquantitative lipid simulations. *J. Phys. Chem. B.* 108:750–760.
51. Marrink, S. J., H. J. Risselada, …, A. H. de Vries. 2007. The MARTINI force field: coarse grained model for biomolecular simulations. *J. Phys. Chem. B.* 111:7812–7824.
52. López, C. A., Z. Sovova, …, S. J. Marrink. 2013. Martini force field parameters for glycolipids. *J. Chem. Theory Comput.* 9:1694–1708.
53. Melo, M. N., H. I. Ingólfsson, and S. J. Marrink. 2015. Parameters for Martini sterols and hopanoids based on a virtual-site description. *J. Chem. Phys.* 143:243152.
54. Gu, R.-X., H. I. Ingólfsson, …, D. P. Tieleman. 2017. Ganglioside-lipid and ganglioside-protein interactions revealed by coarse-grained and atomistic molecular dynamics simulations. *J. Phys. Chem. B.* 121:3262–3275.
55. Wassenaar, T. A., H. I. Ingólfsson, …, S. J. Marrink. 2015. Computational lipidomics with *insane*: a versatile tool for generating custom membranes for molecular simulations. *J. Chem. Theory Comput.* 11:2144–2155.
56. Pronk, S., S. Páll, …, E. Lindahl. 2013. GROMACS 4.5: a high-throughput and highly parallel open source molecular simulation toolkit. *Bioinformatics.* 29:845–854.
57. de Jong, D. H., S. Baoukina, …, S. J. Marrink. 2016. Martini straight: boosting performance using a shorter cutoff and GPUs. *Comput. Phys. Commun.* 199:1–7.
58. Bussi, G., D. Donadio, and M. Parrinello. 2007. Canonical sampling through velocity rescaling. *J. Chem. Phys.* 126:014101.
59. Parrinello, M., and A. Rahman. 1981. Polymorphic transitions in single crystals: a new molecular dynamics method. *J. Appl. Phys.* 52:7182–7190.
60. Bremer, P.-T., G. H. Weber, …, J. B. Bell. 2010. Analyzing and tracking burning structures in lean premixed hydrogen flames. *IEEE Trans. Vis. Comput. Graph.* 16:248–260.
61. Bennett, J. C., V. Krishnamoorthy, …, P.-T. Bremer. 2011. Feature-based statistical analysis of combustion simulation data. *IEEE Trans. Vis. Comput. Graph.* 17:1822–1831.
62. Michaud-Agrawal, N., E. J. Denning, …, O. Beckstein. 2011. MDAnalysis: a toolkit for the analysis of molecular dynamics simulations. *J. Comput. Chem.* 32:2319–2327.
63. Chavent, M., T. Reddy, …, M. S. P. Sansom. 2014. Methodologies for the analysis of instantaneous lipid diffusion in MD simulations of large membrane systems. *Faraday Discuss.* 169:455–475.
64. Marrink, S. J., A. H. de Vries, …, S. R. Wassall. 2008. Cholesterol shows preference for the interior of polyunsaturated lipid membranes. *J. Am. Chem. Soc.* 130:10–11.
65. Bennett, W. F. D., J. L. MacCallum, …, D. P. Tieleman. 2009. Molecular view of cholesterol flip-flop and chemical potential in different membrane environments. *J. Am. Chem. Soc.* 131:12714–12720.
66. Honerkamp-Smith, A. R., S. L. Veatch, and S. L. Keller. 2009. An introduction to critical points for biophysicists; observations of compositional heterogeneity in lipid membranes. *Biochim. Biophys. Acta.* 1788:53–63.
67. Levental, I., and S. Veatch. 2016. The continuing mystery of lipid rafts. *J. Mol. Biol.* 428 (24 Pt A):4749–4764.
68. Levental, I., F. J. Byfield, …, P. A. Janmey. 2009. Cholesterol-dependent phase separation in cell-derived giant plasma-membrane vesicles. *Biochem. J.* 424:163–167.
69. Risselada, H. J., and S. J. Marrink. 2008. The molecular face of lipid rafts in model membranes. *Proc. Natl. Acad. Sci. USA.* 105:17367–17372.
70. Putzel, G. G., M. J. Uline, …, M. Schick. 2011. Interleaflet coupling and domain registry in phase-separated lipid bilayers. *Biophys. J.* 100:996–1004.

71. Perlmutter, J. D., and J. N. Sachs. 2011. Interleaflet interaction and asymmetry in phase separated lipid bilayers: molecular dynamics simulations. *J. Am. Chem. Soc.* 133:6563–6577.

72. Fujimoto, T., and I. Parmryd. 2017. Interleaflet coupling, pinning, and leaflet asymmetry-major players in plasma membrane nanodomain formation. *Front. Cell Dev. Biol.* 4:155.

73. Shevchenko, A., and K. Simons. 2010. Lipidomics: coming to grips with lipid diversity. *Nat. Rev. Mol. Cell Biol.* 11:593–598.

74. Clark, J., K. E. Anderson, …, P. T. Hawkins. 2011. Quantification of PtdInsP3 molecular species in cells and tissues by mass spectrometry. *Nat. Methods.* 8:267–272.

75. Castillo, N., L. Monticelli, …, D. P. Tieleman. 2013. Free energy of WALP23 dimer association in DMPC, DPPC, and DOPC bilayers. *Chem. Phys. Lipids.* 169:95–105.

76. Xie, H., K. T. McDonnell, and H. Qin. 2004. Surface reconstruction of noisy and defective data sets. *In* Proceedings of the VIS '04 Conference on Visualization. IEEE Computer Society, Washington, DC, pp. 259–266.

77. Kazhdan, M., M. Bolitho, and H. Hoppe. 2006. Poisson Surface Reconstruction. *In* Eurographics Symposium on Geometry Processing. K. Polthier and A. Sheffer, eds. Eurographics Association, pp. 61–70.

78. Floater, M. S., and K. Hormann. 2005. Surface parameterization: a tutorial and survey. *In* Advances in Multiresolution for Geometric Modelling. N. A. Dodgson, M. S. Floater, and M. A. Sabin, eds. Springer), pp. 157–186.

79. Venable, R. M., H. I. Ingólfsson, …, R. W. Pastor. 2017. Lipid and peptide diffusion in bilayers: the Saffman-Delbrück model and periodic boundary conditions. *J. Phys. Chem. B.* 121:3443–3457.

Biophysical Journal, Volume *113*

Supplemental Information

Computational Lipidomics of the Neuronal Plasma Membrane

Helgi I. Ingólfsson, Timothy S. Carpenter, Harsh Bhatia, Peer-Timo Bremer, Siewert J. Marrink, and Felice C. Lightstone

Supporting Material for:

Computational lipidomics of the neuronal plasma membrane

Helgi I. Ingólfsson, Timothy S. Carpenter, Harsh Bhatia, Peer-Timo Bremer, Siewert J. Marrink, and Felice C. Lightstone

Supplementary Methods

Lipid compositions

For the composition of the **Average** plasma membrane (PM) we used the idealized mammalian PM mixture described in (1). The **Average** mixture is composed of 63 different Martini lipid types asymmetrically distributed between the outer and inner membrane leaflets (Figure 1A). Different regions within the brain, and different cell types can have diverse membrane compositions (2-4). However, properly isolating large numbers of specific cell types can be extremely difficult. Thus, given the type of neural lipidomic data available, it was more sensible to construct a model that possessed the general properties of membranes found within the brain. The **Brain** composition represents the lipid composition of human brain tissue or more specifically a typical human neuronal PM mixture. The lipid compositions between different tissue types can vary greatly (5, 6) but specific numbers are hard to determine as a cell membrane lipid compositions can vary with cell type, age, diet, environment and disease state (5, 7-12). To capture a **Brain** PM composition, we did not base our composition on a single brain lipidomic study but a consensus from a number of studies (6, 13-24), and how those vary compared to the **Average** mixture. An overview of the **Brain** and the **Average** compositions is given in Figure 1. The specific lipid types used, their ratio in the outer/inner leaflets, and the lipid counts in the simulations are listed in Table S1. The average percentages of the main headgroup types were adjusted to match average consensus values from (13, 14, 16, 17, 21-24). The main differences being that the **Brain** has a significantly higher cholesterol content. The **Brain** mixture also has less PC and more PE. The **Brain** has less SM but includes cerebrosides that are not present in the **Average** model. PIPs and PI lipids can be hard to resolve in lipidomic studies (25, 26) and were kept at similar concentration as in the **Average** mixture. Additionally, the tail length distributions and tail saturation was adjusted based on reported distribution of PC, PE and SM lipids in (6, 18, 20, 21) as well as overall saturated, monounsaturated, and polyunsaturated distributions from (6, 20).

Force fields

The Martini coarse-grain (CG) model (27, 28) was used for all simulations and all the lipid force fields used can be found at the Martini portal (www.cgmartini.nl). The newest available lipid model was used in all cases except where indicated. New lipid parameters were constructed according to the standard Martini 2.0 lipid building blocks and rules (27, 28) as detailed in (1, 29) using the *lipid-martini-itp-v06.py*; available at the at the Martini portal. The names as well as the Martini CG tail bead composition of all the lipids used in the average mammalian plasma membrane (**Average**) and average neuronal plasma membrane (**Brain**) can be found in Table S1. The Martini O tail, representing oleic acid or palmitoleic acid, was recently updated to CDCC (29) instead of the CCDC used in (1). The **Average** mixture is used unmodified from (1) and therefore has the old arrangement, but the new arrangement was tested for the **Average** mixture in the control simulation **Average new all**. The linker for the lyso lipids has also been updated and, similarly, the old arrangement was kept in in the **Average** mixture but the new one used for the **Brain** mixture and the **Average new all** control simulation. The Martini diacylglycerol (DAG) lipids have recently been updated; the GL1 bead type changed from Nda to P1 to better represent the polarity of the glycerol. This change affects the flip-flop rate of the DAG lipids. For direct comparison of the flip-flop rates the old DAG parameters were used in the main simulations but a control simulation with the new parameters was done (**Average new all**). A modified version of the Martini GM1 and GM3 parameters were recently published that better match the size of ganglioside clusters seen with the GROMOS atomistic force field (30). The original GM1/GM3 parameters (1, 31) were used in the main simulations but the modified parameters were tested in a few control simulations (**Average new all**, **Average new GM**, and **Brain new GM**). The cerebroside lipids in the average neuronal plasma membrane (**Brain**) are modeled by the Martini GS headgroup, a general model for glucosylceramide and galactosylceramide (31).

Detailed simulation set up

The simulations were run using the GROMACS 4.6.7 simulation package (32) using the standard Martini parameters set; called *common* in (33). The simulations were set up following the same protocol as described in (1). In short, the initial configuration of each membrane was set up using the bilayer builder *insane* (29). Each system was energy-minimized (steepest descent, 1500 steps) and simulated for 0.5 ns using a short time step of 10 fs, followed by production runs using a time step of 20 fs. In the production runs large membrane undulations were restricted using weak position restraints (2 kJ mol^{-1} nm^{-2}) on the PO4 bead Z-direction of DPPC, POPC and PIPC lipids in the outer leaflet; see Ingólfsson *et al.* (1) supplementary information for control simulations exploring the effects of these restraints. To explore the effects of undulations simulations with no restraints and weaker restraints (0.2 kJ mol^{-1} nm^{-2}) were also run. The number of lipids in the outer/inner leaflet of each bilayer mixture was adjusted based on independent 1 μs long simulation with symmetrical composition of each leaflet. In these simulations bilayer undulations were suppressed to get better estimates of the average area per

lipid without undulations; this was done by imposing the same Z-directional position restraints as above but with a force constant of 100 kJ mol^{-1} nm^{-2}. The cholesterol distribution between the outer/inner leaflet was equilibrated using the same protocol as described in (1). The initial mixture was started with 50/50 cholesterol distribution: average area per lipid was measured in a pair of symmetrical outer/inner mixture simulations; asymmetrical simulations setup with adjusted number of lipids in either leaflet; the cholesterol distribution was allowed to equilibrate for a few μs; cholesterol leaflet distribution was measured and used as the new initial values for the next round of simulations. This process was iterated until the initial cholesterol concentration was stable.

The final lipid numbers for the large (~20,000 lipids) **Average** and **Brain** simulations are listed in Table S1. The smaller (~6,000 lipids) control simulations have the same relative lipid ratios as the larger simulations. Additionally, the simulations include counter ions, 150 mM NaCl, and ~300,000 Martini water molecules for the larger simulations and ~100,000 for the smaller. The simulations were run at 310 K, with τ_T = 1.0 ps, controlled with the velocity rescaling thermostat (34) and at 1 bar semi-isotropic pressure, with τ_p = 5.0 ps, controlled using the Parrinello-Rahman barostat (35). The larger simulations were run for 80 μs and the smaller control simulations for 50 μs. Additionally, simulations with no or weaker undulation restraints were run for 5 μs starting from the larger simulations at 75 μs.

All simulation times reported are actual times simulated and were not scaled. CG models have less degrees of freedom compared to their atomistic counterparts and therefore normally less friction which leads to overall faster dynamics. The effective speedup varies depending on the molecule and system in question but for Martini the speedup is often pegged at around 4-fold (28).

Analysis

The average area per lipid (A_l) of the outer and inner leaflet of the **Average** and **Brain** lipid mixtures were estimated individually in simulations of symmetric bilayers containing 6,000-7,000 lipids of the outer or the inner lipid mixtures. The simulations were kept flat using strong position restraints, force constant 100 kJ mol^{-1} nm^{-2} (see above) and simulated for 1 μs. The A_l was estimated as the average box area of the last 100 ns divided by the number of lipids in each leaflet; resulting in outer/inner A_l of 0.513 / 0.553 and 0.460 / 0.485 nm^2 for the **Average** and **Brain**, respectively, with standard error ~0.001 nm^2.

A lipid flip-flop is defined when a lipid moves from one leaflet to another and flip-flop rates were measured as described in (1). The **Brain** membrane thickness fluctuates somewhat more than the **Average** membrane, therefore, we extended the cutoff length for what is considered within a leaflet to 1.1 nm removing spurious flip-flop event. Lipid flip-flop rates were calculated for all lipid classes and averaged over the last 10 μs of the simulations. During the simulations, only the CHOL, DAG and ceramide (CER) lipid types flip-flopped. The measured flip-flop rates per molecule are: CHOL 7.290±0.018 x 10^6 s^{-1}, DAG 7.662±0.049 x 10^6 s^{-1}, and

CER 2.7±0.6 x 10^4 s^{-1} and CHOL 4.820±0.004 x 10^6 s^{-1}, DAG 2.800±0.074 x 10^6 s^{-1}, and CER 1.5±0.5 x 10^4 s^{-1} for the **Average** and **Brain** membranes, respectively. The error is estimated as the standard error of the mean when the last 10 μs of the simulations were split in three equally sized blocks and analyzed separately. Flip-flop rates for the alternative parameter control simulations are given in the legend of Figure S7.

Cholesterol fraction in the bilayer middle was determined by counting the number of cholesterols whose ROH bead was within 0.8 nm of the bilayer center averaged over the last 10 μs of the simulations.

In order to explore undulation in lipid bilayers, we project the headgroups on an approximate surface representing the bilayer membrane, and compute properties, such as area per lipid, curvature, and normals on these projections. In particular, given the positions of the headgroups, P_i, the undulations in bilayers can be captured using the following steps:

1. The lipid bilayer leaflets were defined using the MDAnalysis leaflet finder (36). The top headgroup bead was used for all lipids, except for the Glyco, PI and PIP lipids; where the GM1 and C1 beads were used. Initially, the outer and inner leaflets were defined from all non-flip-flopping lipids, then for each simulation frame the flip-flopping lipids with headgroup beads within 1.2 nm of either leaflet were included in those leaflets.
2. Surface fitting requires consistently oriented normal vectors n_i for each P_i. Normals are computed using the principal component analysis (PCA) in the local neighborhood around P_i, and oriented consistently through a depth-first traversal of the distance-based minimum spanning tree of P_i (37). Finally, using the Poisson reconstruction method (38) on (P_i, n_i), an approximate surface, Ψ, is obtained as a representative of the bilayer membrane. The Poisson reconstruction is a global solution, and is chosen because it provides a natural way to smooth noisy fluctuations in the given points, while maintaining the overall shape of the surface.
3. The obtained surface, Ψ, is then projected onto the 2D Euclidean plane, giving Ψ° using discrete harmonic mapping (39), which allows keeping the angular distortion to a minimum. The given positions of the headgroups, P_i, are then projected on Ψ, giving P_i^{Ψ}. Using the surface projection obtained above, these points are then projected to the 2D plane, giving P_i°. Using two projections, i.e., $P_i \rightarrow P_i^{\Psi} \rightarrow P_i^{\circ}$ allows minimizing distortion to the curvature and area per lipid, and thus, provides better approximation of the said properties, as compared to directly projecting the points onto the 2D plane.
4. A periodic 2D Delaunay triangulation is then performed on P_i°, which establishes a neighborhood graph, $\mathcal{T}$ between P_i°, and hence, P_i. Given the connectivity $\mathcal{T}$ on the original points P_i^{Ψ}, we compute bilayer normals, N_i. Note that, using the triangulation enables a more accurate estimation of bilayer normals as compared to those computed in Step 2. Finally, we quantify the undulations in bilayers as the angle between the bilayer normal N_i and upward z-axis, i.e., $b_i = \cos^{-1}(|N_i^z|)$.

Lipid tail order was evaluated using the lipid tail order parameter (*S*), defined as:

$$S = \frac{1}{2}(3\langle(\cos\theta)^2\rangle - 1).$$

where θ is the angle between the vector along a particular lipid tail bond and the bilayer normal at the given lipid. The bilayer normal, N_i, is defined from the bilayer surface as described above. Tail order was evaluated for each lipid tail of each lipid type separately for the outer and inner leaflets, except for DAG and CER lipids that flip-flop between the leaflets. The absolute average order parameter of a particular lipid tail up to the lipids linker (AM or GL beads) was used for comparing the different tails overall order/flexibility, see Table S2. The weighted average order parameters (excluding lipids that flip-flop) are: **Average** [0.435,0.374] / [0.430,0.301] and **Brain** [0.487,0.391] / [0.444,0.224], respectively for the [sn-1, sn-2] tails in the outer/inner leaflet. For both the **Average** and **Brain** membranes the inner leaflet tails are less ordered than the outer leaflet but the difference is significantly greater in the **Brain** membrane. The increased tail order (excluding DAG and CER lipids) in the outer with respect to the inner is 11% for the **Average** and 31% for the **Brain**. The lipid tail lengths vary between the different lipid types, therefore, we also evaluated the tail order using *S* at pos3 (between beads 2 and 3, present in all non-sterol lipids). Combining the lipid tails and calculating the weighted average between all lipids at pos3 the order in the outer/inner leaflet is: **Average** 0.412/0.349 and **Brain** 0.445/0.301, with a weighted error of ~0.001 or less. That is an increase of 18% and 48% for the outer over the inner leaflet of the **Average** and **Brain** membranes, respectively.

The lipid lateral diffusion coefficients (*D*) were calculated from the mean square displacement (MSD) of the molecules in each membrane plane. The GROMACS g_msd tool was used over the last 10 μs of the simulations to obtain the diffusion coefficients and errors. The MSD curves, excluding the first and last 10% of each curve, were fitted to $y = 4Dt + c$, to obtain *D*. For each lipid type the GL1, AM1 or ROH bead was used for the glycerol, ceramide or cholesterol lipids, respectively. All diffusion values are reported in Table S3. Note, lipid diffusion coefficients are reported as is and no correction is applied for overestimates due to the larger effective simulation speed of CG simulations (28) or underestimates due to the periodically bound finite system sizes (40).

Lipid neighbor counting was used to evaluate non-ideal lipid mixing, Figure S2. Lipids in the same leaflet and within a 1.5 nm radius XY plane cut-off were considered as neighbors, values were averaged over the last 10 μs of the simulations and their relative enrichment/depletion compared to random mixing, see detailed description of method in (1).

For an indicator of overall lipid mobility lipid root mean square fluctuations (RMSF) over the last 2 μs were used (Figure S3A and B). RMSF were calculated for all non-flip-flopping lipids based on their GL1 or AM1 beads using the GROMACS g_rmsf tool and plotted onto of their corresponding beads at 80 μs.

Bilayer thickness plots were created by calculating the local average distance in the Z-direction between the phosphate beads (PO4) and the first headgroup bead of the glycolipids (GM1 or C1) in the two leaflets, averaged over the last 2 μs the simulations, and plotted using the tool g_thickness (41). The plot was subsequently drawn using bins of 1.42 x 1.42 nm and a

color scale varying from 3.6 to 4.4 nm (Figure S3C). Average bilayer thickness was determined in five blocks over the last 10 μs the simulations resulting in 4.109±0.001 nm for the **Average** and 4.057±0.002 for the **Brain**.

Lipid flow analysis was carried out on the last 2 μs of the simulations using the methodology described by Chavent *et al.* (42). The trajectories were firstly pre-processed to remove the center of mass motion and subjected to low-pass filtering to remove high frequency noise using the GROMACS g_filter function. The filtering of the systems was carried out over a time scale of 200 ns. The leaflet correlation function, $Cl(t)$, at time t, as taken from Chavent *et al.* (42), defined as:

$$C_{l(t)} = \frac{1}{N}\sum_{i=1}^{N} \frac{\overrightarrow{u_{i(t)}} \cdot \overrightarrow{v_{i(t)}}}{|\overrightarrow{u_{i(t)}}||\overrightarrow{v_{i(t)}}|}.$$

The system is divided into a grid of cells, where N is the number of non-empty cells in the grid, and · denotes the scalar product of vectors $u_{i(t)}$ and $v_{i(t)}$ as defined as the distance between the center of mass of the constituent lipids at time $t+dt$ and at time t. $u_{i(t)}$ and $v_{i(t)}$ are the lower and upper leaflet vectors.

Lipid clustering based on cholesterol density. To define lipid domains a kernel density estimator was used to define a cholesterol density. After several experiments with different kernel bandwidths a Gaussian kernel $K(x,y) = \exp(-||x-y|| / s^2)$ with s = 3 nm was chosen as a good balance between smoothing local variations and detecting small, transient domains. Given the density value at each cholesterol a periodic Delaunay triangulation was computed using the CGAL library (Computational Geometry Algorithms Library, www.cgal.org). Finally, domains for high/low cholesterol were defined using density thresholds. More specifically, regions of high cholesterol were defined as connected components of the Delaunay triangulation above a given threshold and regions of low cholesterol symmetrically as connected components below a given threshold. To efficiently explore the impact of different threshold choices the topological analysis framework described in (43, 44) was used to encode all domains for all possible thresholds in form of a so called merge-/split-tree. This is equivalent to a traditional isosurface extraction but computationally more efficient. Domain size was defined as the number of cholesterols part of each lipid domain.

The cross-correlations between the cholesterol density of the outer/inner leaflet was calculated for every 5 ns of the simulations. The cholesterol densities were resampled to a 128x128 pixel grid and the Pearson correlation calculated between the leaflets, Figure 3C. Average values over the last 10 μs of the simulations are 0.45±0.01 and -0.14±0.01 for the **Average** and **Brain** mixtures, respectively, where the error was estimated by splitting the last 10 μs into four equal parts and calculating the standard error between the averages of the parts.

Density maps were calculated in the bilayer XY-plane, with a bin size of ~2 nm. One bead per lipid was used, as indicated, and averaged over the last 2 μs of the simulations.

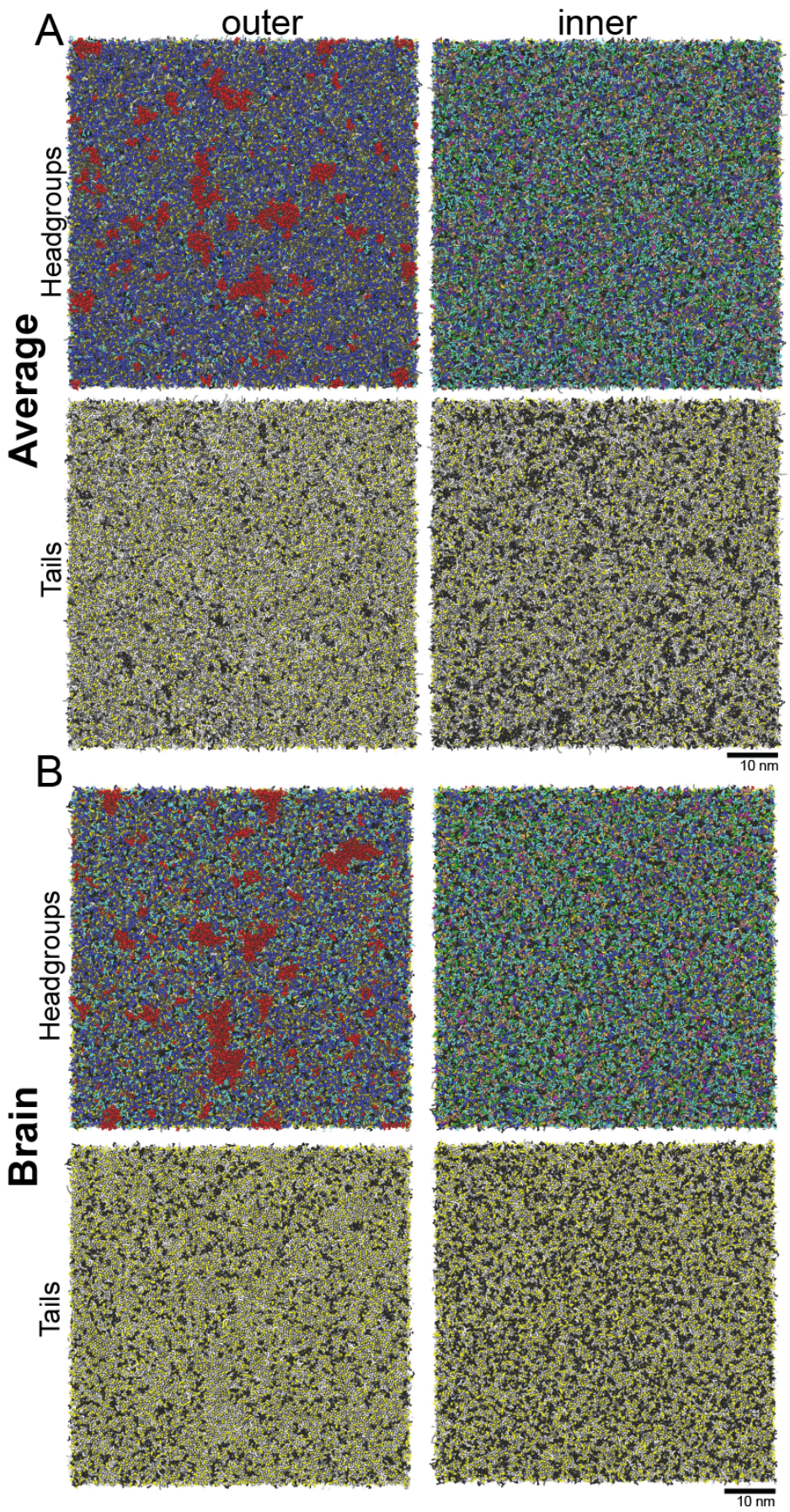
A
outer
inner
Average
Headgroups
Tails
10 nm
B
Brain
Headgroups
Tails
10 nm

Figure S1. Lipid headgroup and tail configuration. Snapshots of the outer/inner leaflets of the **Average** (A) and **Brain** (B) mixtures after 80 μs of simulation. The snapshots are shown with the headgroups and without to illustrating the tails; the color scheme for the lipid headgroups and tails is the same as used in Fig. 1. The lipids are colored by type (PC, blue; SM, gray; PE, cyan; Glyco, red; PIPs, magenta; PI, pink; PS, green; PA, white; CE, ice blue; DG, brown; LPC, orange; CHOL, yellow,) and tails by number of saturations (0, white; 1, light gray; 2, dark gray; 3-6, black) and cholesterol shown in yellow.

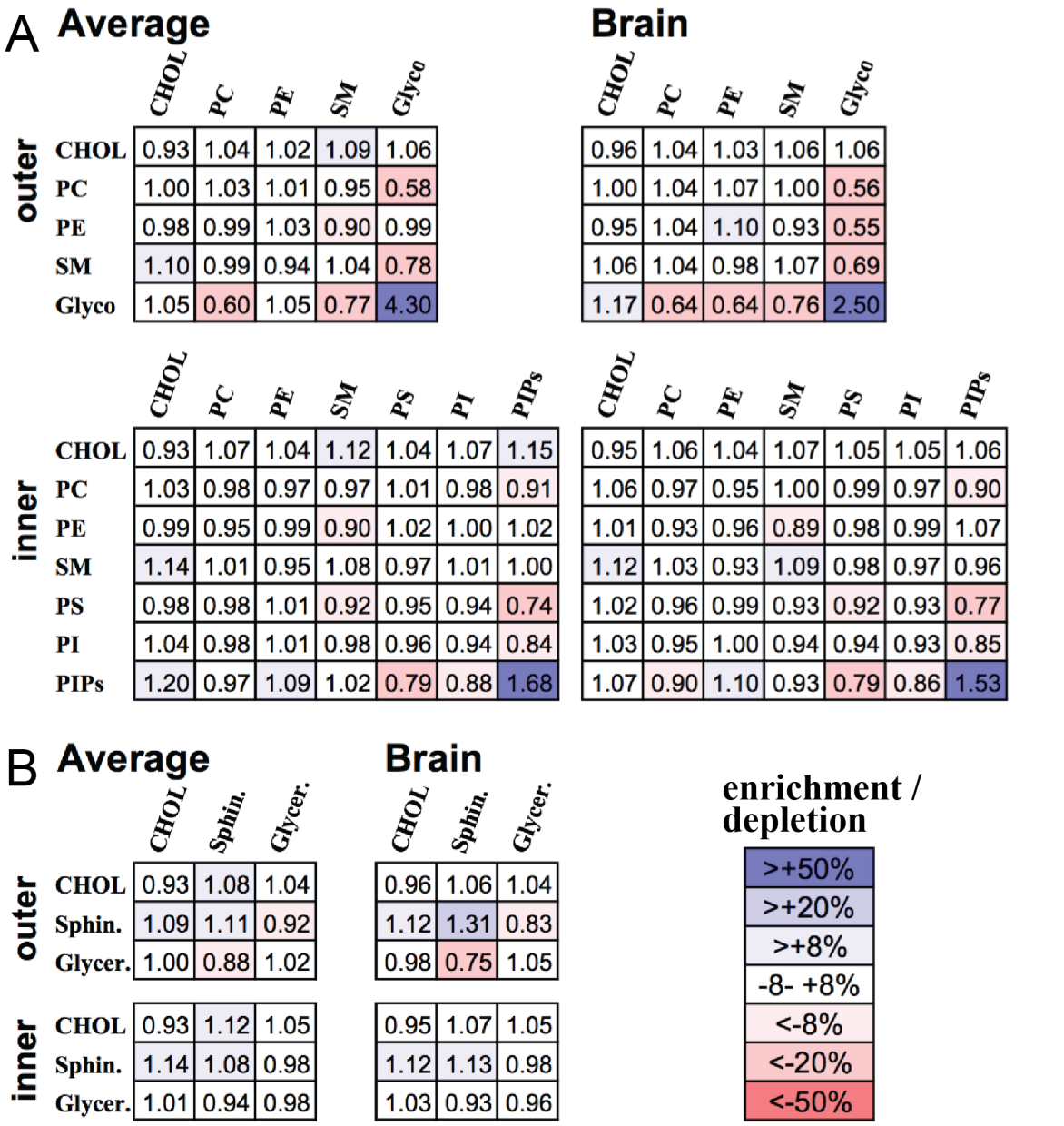

Figure S2. Non-ideal lipid mixing. Number of neighboring lipids (within 1.5 nm) grouped by headgroup type (A) and linker type (B); where Sphin. are sphingolipids and Glycer. are glycerolipids. Values are averaged over the last 10 μs of the simulation and normalized to the weighted average number of neighbors of each type to highlight the relative enrichment/depletion of those lipids. Standard errors for all counts are <0.03.

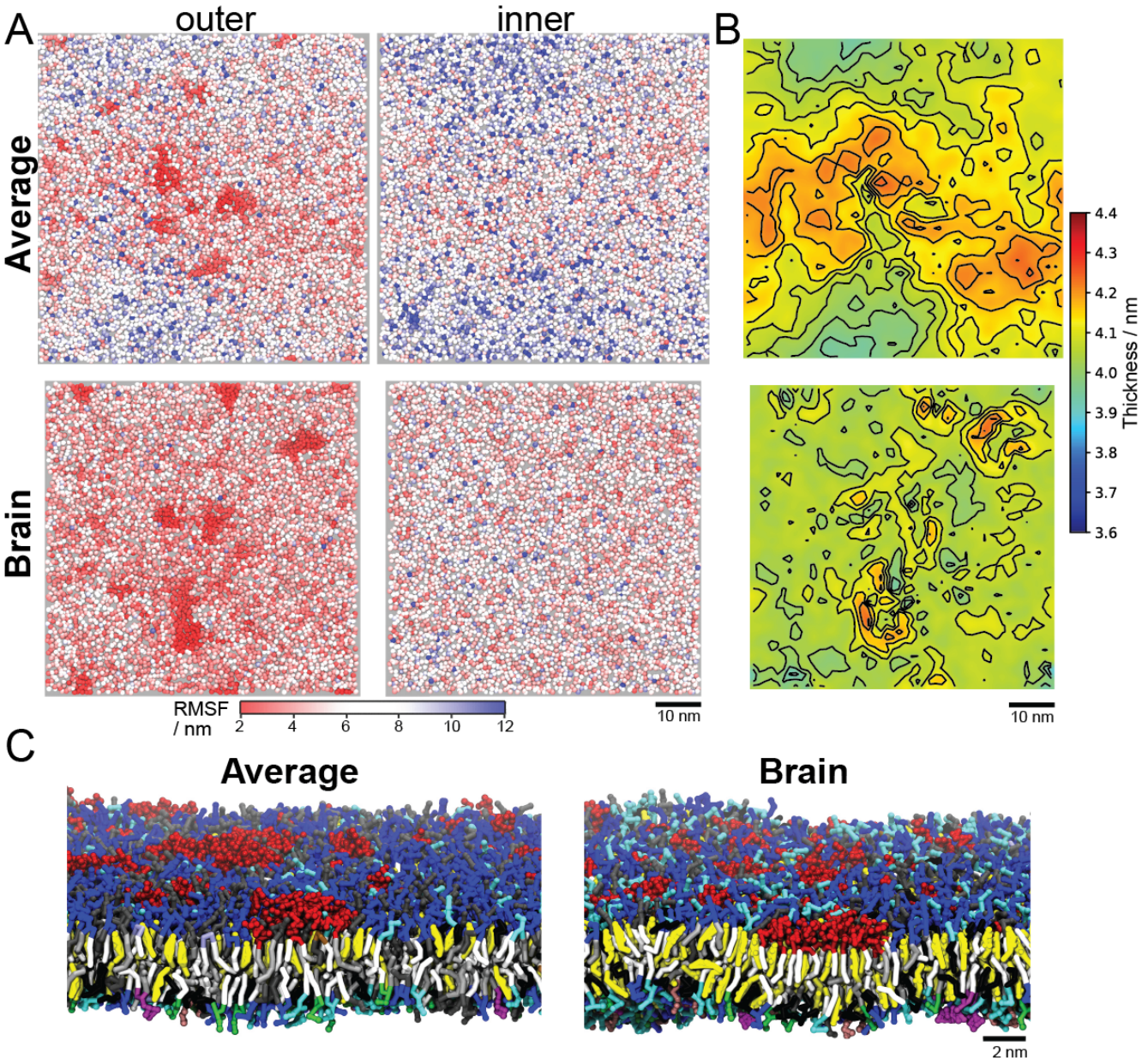

Figure S3. Membrane domain properties. (A) PM lipid root mean square fluctuations (RMSF) are shown to indicate differences in lipid mobility. RMSF values were calculated for the GL1 and AM1 linker beads of all non-flip-flopping lipids over the last 2 μs of the simulations and plotted onto the bead positions at 80 μs. Note, the dark red clusters in the outer leaflets of both the **Average** and **Brain** corresponds to clusters of glycolipids. (B) 2D PM thickness plots, calculated between all PO4 beads in either leaflets. The average thickness is similar between the PMs (4.11 nm for the **Average** and 4.06 nm for the **Brain**). (C) Representative zoomed in snapshots for the **Average** and **Brain** PM side and outer leaflet. The lipids are colored in the same way as in Fig. 1. Somewhat tighter packing and more local undulations can be seen in the **Brain** mixture, despite same method for reducing large undulations.

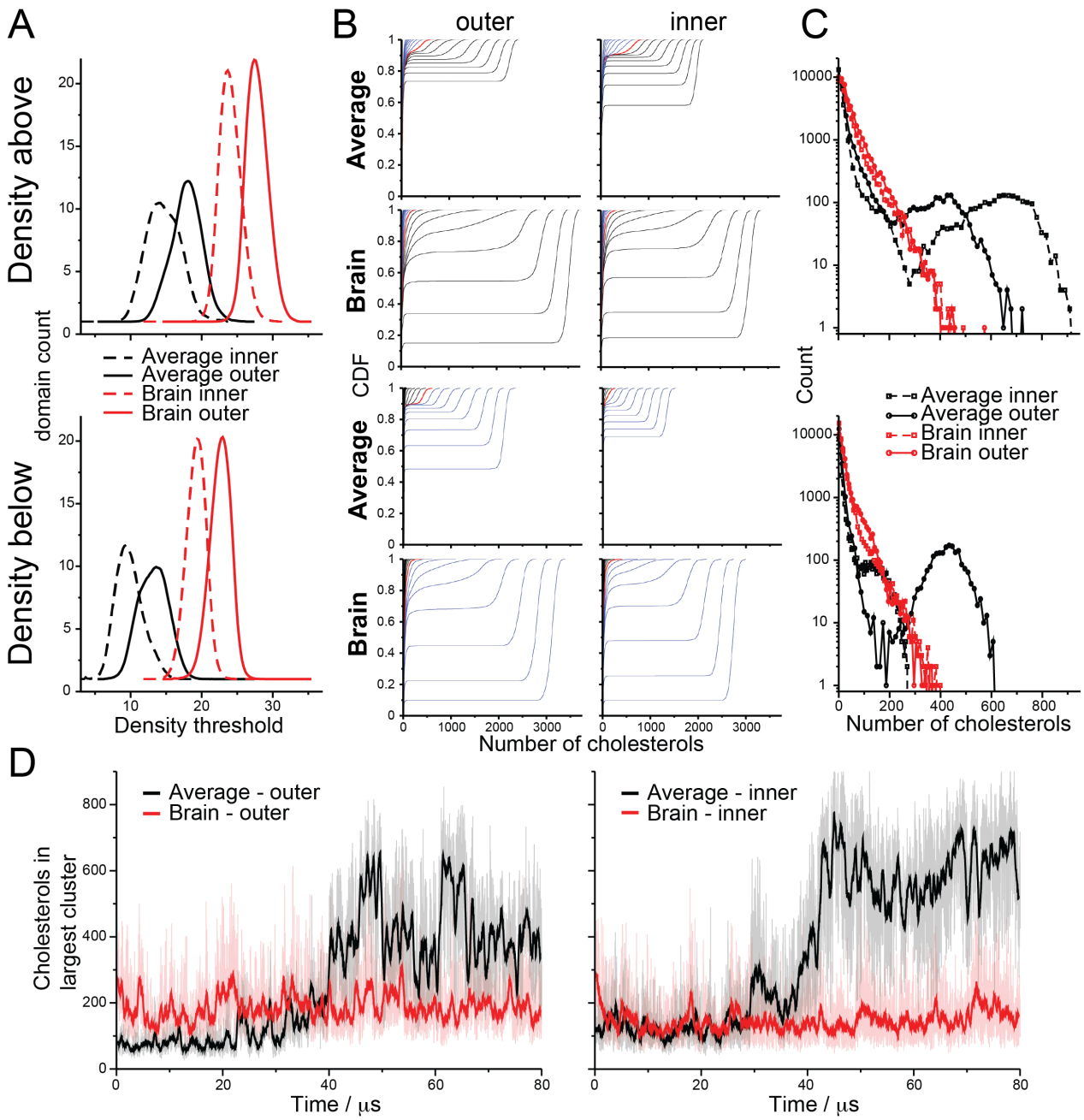

Figure S4. Cholesterol density cluster parameter sensitivity. (A) For the outer (solid lines) and inner (dotted lines) leaflets of the **Average** (black) and **Brain** (red) membranes the average number of domains per frame were computed over the last 10 μs for a range of possible thresholds. The top panel is numbers with higher density than specified (high-density regions) and the bottom panels is lower density than specified (low-density regions). (B) The cumulative distribution function (CDF) of domain "sizes" (number of cholesterols) for a range of thresholds. The selected threshold (max of A) is shown in red: [18.1 , 13.6] / [14.0, 9.4] and [27.4, 23.0] / [23.7, 19.4] for the **Average** and **Brain** [high, low] outer/inner, respectively. Additionally, x8 lower thresholds in blue and x8 higher thresholds in black are shown; deviating from the selected threshold in 0.5 increments. (C) Histograms of the domain sizes (in number of cholesterols) at the selected threshold. (A-C) Are averaged over the last 10 μs of the simulations. (D) Size (in

number of cholesterols) of the largest high-density domain in each frame of the **Average** and **Brain** simulations. Shown for every 5 ns (dimmed lines) and average over 500 ns (bold lines).

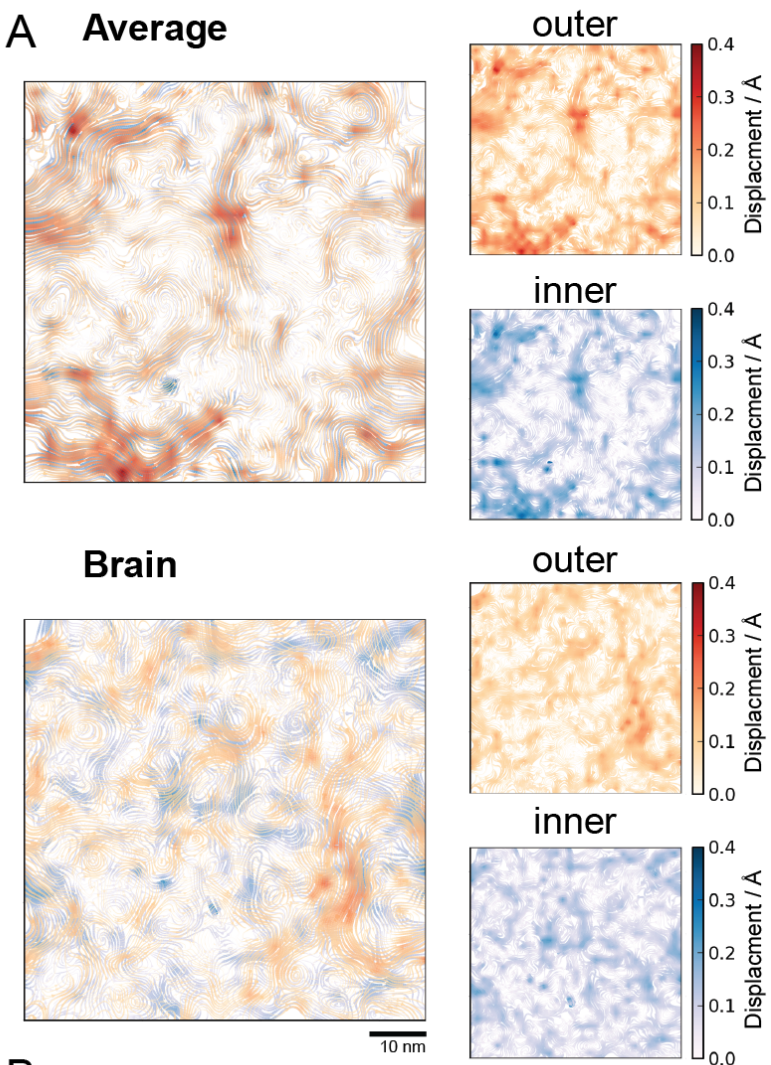

B

Window / ns	Average	Brain
8	0.91	0.45
16	0.93	0.42
40	0.95	0.32

Figure S5. Lipid flow analysis. (A) Using sampling over the final 200 ns of each PM simulation, the mean-squared displacement for each lipid leaflet is calculated and tracked using the *flow* methodology (see SI Methods). The average displacement is shown for both the outer (red scale) and inner (blue scale) leaflets separately in the smaller images, and are overlaid together in the larger images to highlight correlations in regions of similar displacement. (B) The inter-leaflet lipid flow correlation is shown as a function temporal smoothing window (ns) to illustrate that the lipid flow of the **Average** PM mixture is highly correlated but the **Brain** mixture not so much, especially over longer timescales.

Figure S6A-B

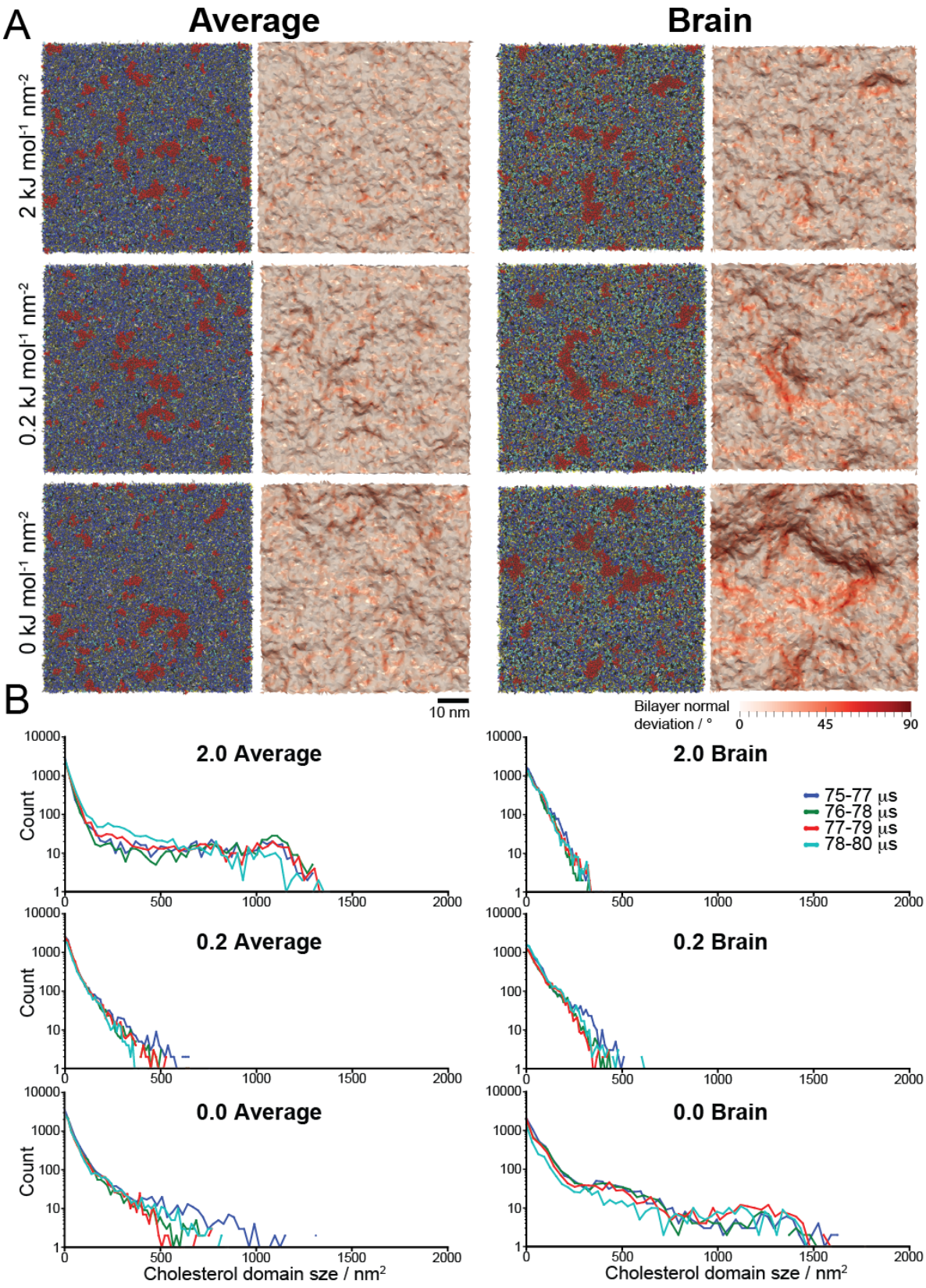
A
Average
Brain
2 kJ mol-1 nm-2
0.2 kJ mol-1 nm-2
0 kJ mol-1 nm-2
10 nm
Bilayer normal deviation / °
0
45
90
B
2.0 Average
2.0 Brain
0.2 Average
0.2 Brain
0.0 Average
0.0 Brain
75-77 µs
76-78 µs
77-79 µs
78-80 µs
Count
Cholesterol domain sze / nm2

Figure S6C

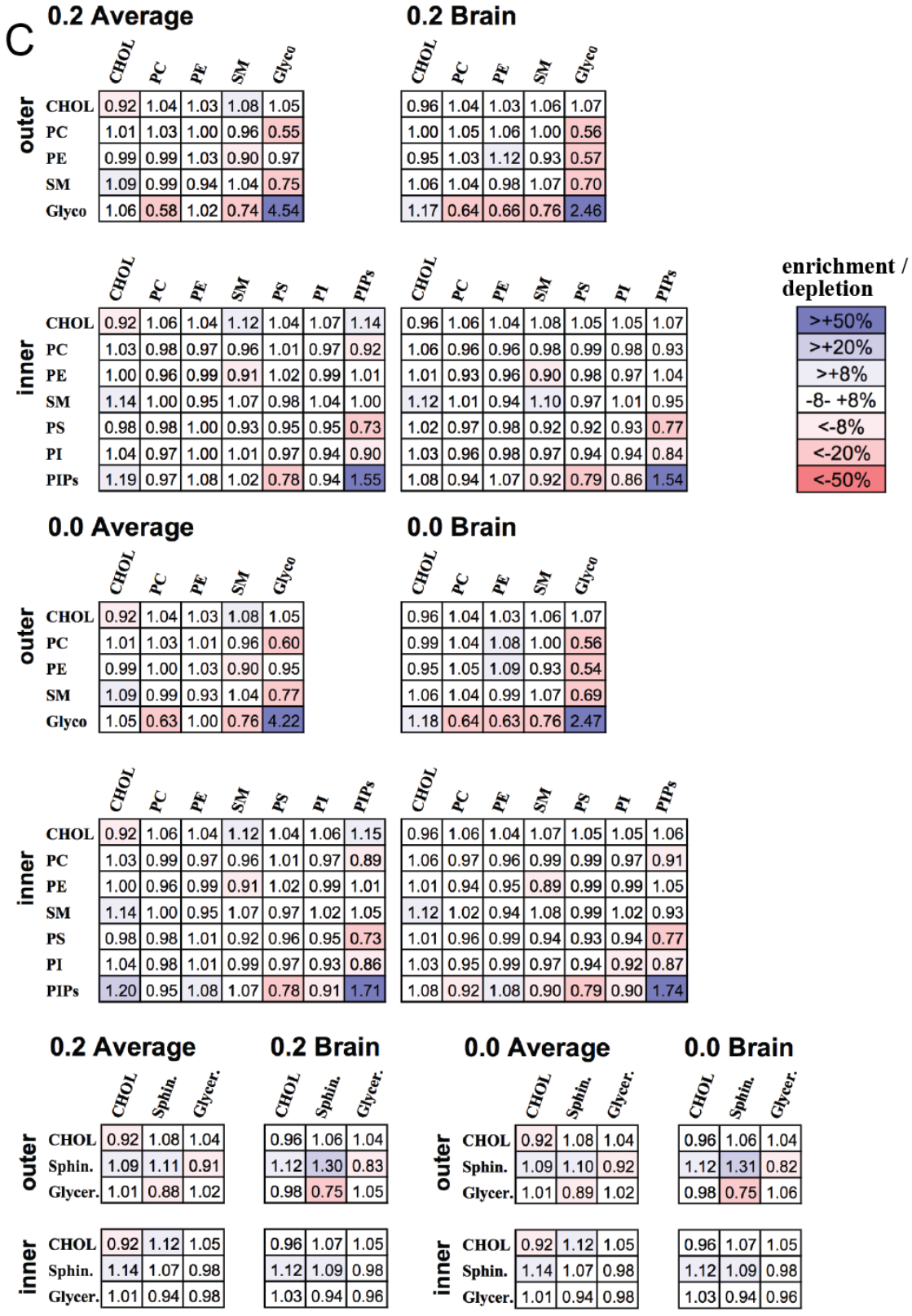
C
0.2 Average
0.2 Brain
outer
inner
CHOL PC PE SM Glyco
CHOL 0.92 1.04 1.03 1.08 1.05
PC 1.01 1.03 1.00 0.96 0.55
PE 0.99 0.99 1.03 0.90 0.97
SM 1.09 0.99 0.94 1.04 0.75
Glyco 1.06 0.58 1.02 0.74 4.54
CHOL 0.96 1.04 1.03 1.06 1.07
PC 1.00 1.05 1.06 1.00 0.56
PE 0.95 1.03 1.12 0.93 0.57
SM 1.06 1.04 0.98 1.07 0.70
Glyco 1.17 0.64 0.66 0.76 2.46
CHOL PC PE SM PS PI PIPs
CHOL 0.92 1.06 1.04 1.12 1.04 1.07 1.14
PC 1.03 0.98 0.97 0.96 1.01 0.97 0.92
PE 1.00 0.96 0.99 0.91 1.02 0.99 1.01
SM 1.14 1.00 0.95 1.07 0.98 1.04 1.00
PS 0.98 0.98 1.00 0.93 0.95 0.95 0.73
PI 1.04 0.97 1.00 1.01 0.97 0.94 0.90
PIPs 1.19 0.97 1.08 1.02 0.78 0.94 1.55
CHOL 0.96 1.06 1.04 1.08 1.05 1.05 1.07
PC 1.06 0.96 0.96 0.98 0.99 0.98 0.93
PE 1.01 0.93 0.96 0.90 0.98 0.97 1.04
SM 1.12 1.01 0.94 1.10 0.97 1.01 0.95
PS 1.02 0.97 0.98 0.92 0.92 0.93 0.77
PI 1.03 0.96 0.98 0.97 0.94 0.94 0.84
PIPs 1.08 0.94 1.07 0.92 0.79 0.86 1.54
enrichment / depletion
>+50%
>+20%
>+8%
-8- +8%
<-8%
<-20%
<-50%
0.0 Average
0.0 Brain
CHOL PC PE SM Glyco
CHOL 0.92 1.04 1.03 1.08 1.05
PC 1.01 1.03 1.01 0.96 0.60
PE 0.99 1.00 1.03 0.90 0.95
SM 1.09 0.99 0.93 1.04 0.77
Glyco 1.05 0.63 1.00 0.76 4.22
CHOL 0.96 1.04 1.03 1.06 1.07
PC 0.99 1.04 1.08 1.00 0.56
PE 0.95 1.05 1.09 0.93 0.54
SM 1.06 1.04 0.99 1.07 0.69
Glyco 1.18 0.64 0.63 0.76 2.47
CHOL PC PE SM PS PI PIPs
CHOL 0.92 1.06 1.04 1.12 1.04 1.06 1.15
PC 1.03 0.99 0.97 0.96 1.01 0.97 0.89
PE 1.00 0.96 0.99 0.91 1.02 0.99 1.01
SM 1.14 1.00 0.95 1.07 0.97 1.02 1.05
PS 0.98 0.98 1.01 0.92 0.96 0.95 0.73
PI 1.04 0.98 1.01 0.99 0.97 0.93 0.86
PIPs 1.20 0.95 1.08 1.07 0.78 0.91 1.71
CHOL 0.96 1.06 1.04 1.07 1.05 1.05 1.06
PC 1.06 0.97 0.96 0.99 0.99 0.97 0.91
PE 1.01 0.94 0.95 0.89 0.99 0.99 1.05
SM 1.12 1.02 0.94 1.08 0.99 1.02 0.93
PS 1.01 0.96 0.99 0.94 0.93 0.94 0.77
PI 1.03 0.95 0.99 0.97 0.94 0.92 0.87
PIPs 1.08 0.92 1.08 0.90 0.79 0.90 1.74
0.2 Average
0.2 Brain
0.0 Average
0.0 Brain
outer
inner
CHOL Sphin. Glycer.
CHOL 0.92 1.08 1.04
Sphin. 1.09 1.11 0.91
Glycer. 1.01 0.88 1.02
CHOL 0.96 1.06 1.04
Sphin. 1.12 1.30 0.83
Glycer. 0.98 0.75 1.05
CHOL 0.92 1.08 1.04
Sphin. 1.09 1.10 0.92
Glycer. 1.01 0.89 1.02
CHOL 0.96 1.06 1.04
Sphin. 1.12 1.31 0.82
Glycer. 0.98 0.75 1.06
CHOL 0.92 1.12 1.05
Sphin. 1.14 1.07 0.98
Glycer. 1.01 0.94 0.98
CHOL 0.96 1.07 1.05
Sphin. 1.12 1.09 0.98
Glycer. 1.03 0.94 0.96
CHOL 0.92 1.12 1.05
Sphin. 1.14 1.07 0.98
Glycer. 1.01 0.94 0.98
CHOL 0.96 1.07 1.05
Sphin. 1.12 1.09 0.98
Glycer. 1.03 0.94 0.96

Figure S6. Bilayer undulation simulations. Starting from the main **Brain** and **Average** PM simulations at 75 μs, simulations were run for 5 μs with either tenfold weaker, or no restraints on bilayer undulations (0.2 and 0.0 kJ mol^{-1} nm^{-2}, respectively), see also Fig. 4. (A) Outer leaflet top view snapshots of the final structure of each simulation are shown. The lipids are colored in the same way as in Fig. 1 and S1. The deviations of the bilayer normal away from the box z-axes (white to red in degrees) are shown on top of the fitted bilayer surfaces. (B) Size histograms of cholesterol enriched domains in the outer leaflet of each simulation, using the threshold that maximizes the number of domains. The histograms were made from 2 μs simulation blocks ranging from the beginning to the end the simulations (75 – 80 μs for the main simulations). (C) Number of neighboring lipids (within 1.5 nm) grouped by headgroup type (top) and linker type (bottom); where Sphin. are sphingolipids and Glycer. are glycerolipids. Values are averaged over the last 2 μs of the simulation and normalized to the weighted average number of neighbors of each type to highlight the relative enrichment/depletion of those lipids. Standard errors for all counts are <0.03. Value for the main simulations, with 2.0 kJ mol^{-1} nm^{-2} undulation restraints are in Fig. S2.

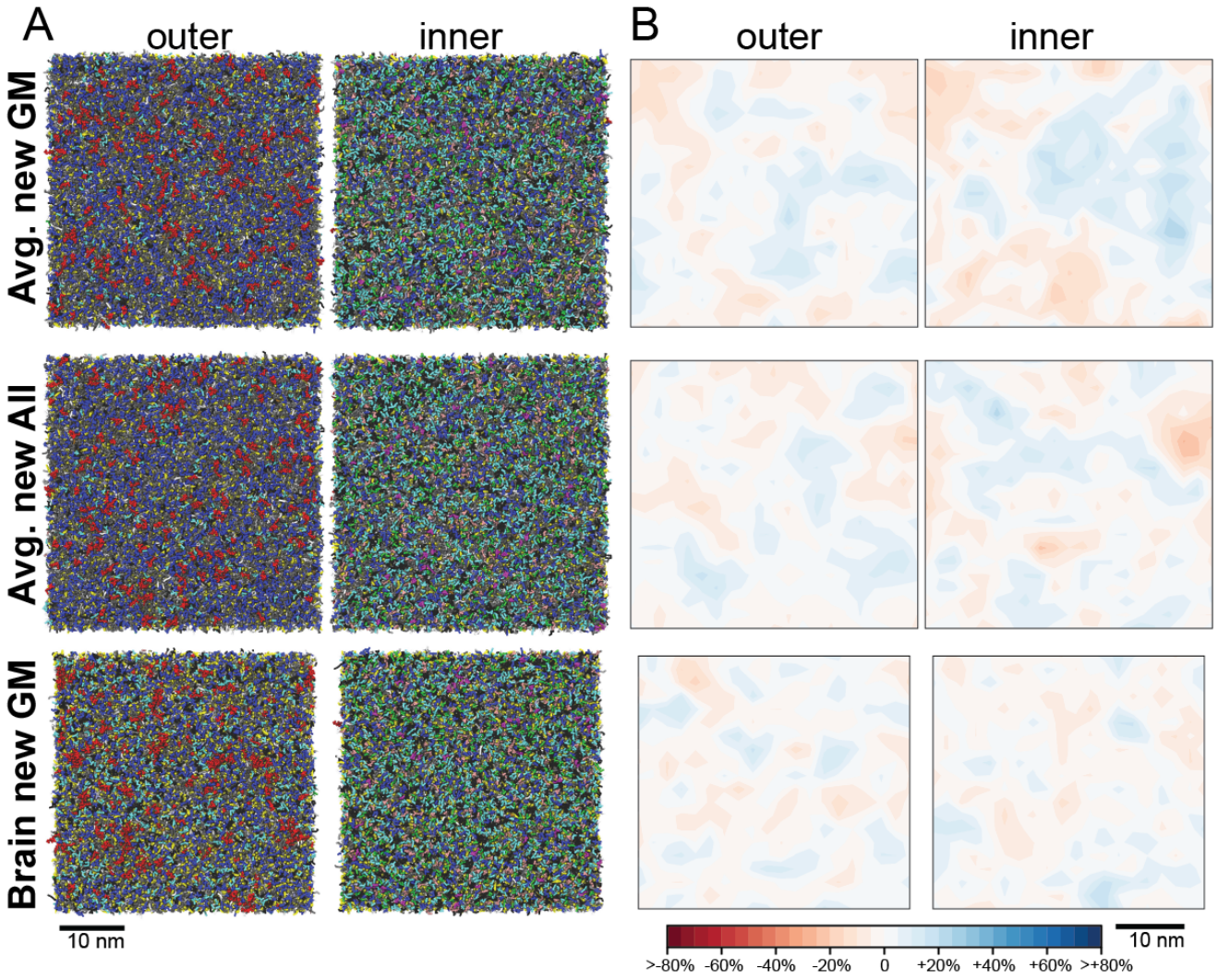

Figure S7. Alternative lipid parameters. Smaller repeat simulations (~6,000 lipids) were run for 50 μs with the recently published alternative parameters for GM1 and GM3 (30) (**Avg. new GM** and **Brain new GM**) as well as an **Average** PM mixture with the all the most up-to-date Martini parameters (**Avg. new All**), see Supplementary Methods. (A) Snapshots of the outer/inner leaflet of the simulations after 50 μs are shown using the same color scheme as in Fig. 1. (B) 2D density maps averaged over the last 200 ns are shown for cholesterol's ROH beads in the inner/outer leaflet of each simulations. Average properties including lipid flip-flop rates were also calculated for these control simulations and were similar as their corresponding **Average** or **Brain** larger simulations. Only CHOL, DAG, and CER lipids flip-flopped and their rates are: CHOL 7.30±0.07 x 10^6 s^{-1}, DAG 6.2±0.2 x 10^6 s^{-1}, and CER 1.5±0.4 x 10^4 s^{-1} (**Avg. new GM**); CHOL 7.79±0.07 x 10^6 s^{-1}, DAG 3.5±0.1 x 10^6 s^{-1}, and CER 1.5±0.4 x 10^4 s^{-1} (**Avg. new All**); and CHOL 4.84±0.02 x 10^6 s^{-1}, DAG 2.8±0.1 x 10^6 s^{-1}, and CER 2±1 x 10^4 s^{-1} (**Brain new GM**).

Table S1 Lipid composition[a]

Lipid tail sn-1	Lipid tail sn-2	Acronym	Average				Brain			
			Outer leaflet count	Outer leaflet mole fraction	Inner leaflet count	Inner leaflet mole fraction	Outer leaflet count	Outer leaflet mole fraction	Inner leaflet count	Inner leaflet mole fraction
Phosphatidylcholine - PC			***outer/inner ratio***		***0.69***	***0.31***			***0.65***	***0.35***
CCCC	CCCC	DPPC					531	0.053	284	0.030
CCCC	CDCC	POPC	1205	0.122	550	0.059	868	0.087	463	0.049
CDCC	CDCC	DOPC	106	0.011	49	0.005	221	0.022	118	0.012
CCCC	CDDC	PIPC	1772	0.179	810	0.087				
CCCC	CDDD	PFPC					59	0.006	32	0.003
CCCC	CDDCC	PEPC	71	0.007	32	0.003				
CCCC	DDDDC	PAPC	283	0.029	129	0.014	463	0.046	247	0.026
DDDDC	DDDDC	DAPC	35	0.004	16	0.002				
CCCC	DDDDDC	PUPC	71	0.007	32	0.003	169	0.017	90	0.010
CDCC	CDDC	OIPC					59	0.006	32	0.003
CDCC	DDDDDC	OUPC					42	0.004	22	0.002
		Total:	**3543**	**0.357**	**1618**	**0.173**	**2412**	**0.242**	**1288**	**0.136**
Phosphatidylethanolamine - PE			***outer/inner ratio***		***0.19***	***0.81***			***0.35***	***0.65***
CCCC	CCDC	POPE	135	0.014	569	0.061	127	0.013	234	0.025
CDCC	CDCC	DOPE	44	0.004	190	0.020				
CCCC	CDDC	PIPE	90	0.009	380	0.041				
CCCC	CDDDC	PQPE	22	0.002	95	0.010				
CCCC	DDDDC	PAPE	124	0.013	522	0.056	312	0.031	574	0.061
DDDDC	DDDDC	DAPE	78	0.008	332	0.036				
CCCC	DDDDDC	PUPE	44	0.004	190	0.020	500	0.050	922	0.097
DDDDDC	DDDDDC	DUPE	22	0.002	95	0.010				
CDCC	CDDC	OIPE					14	0.001	27	0.003
CDCC	DDDDC	OAPE					68	0.007	127	0.013
CDCC	DDDDDC	OUPE					72	0.007	133	0.014
		Total:	559	0.056	2373	0.254	1093	0.110	2017	0.213
Sphingomyelin - SM			***outer/inner ratio***		***0.69***	***0.31***		***0.80***		***0.20***
TCC	CCCC	DPSM	611	0.062	279	0.030	581	0.058	143	0.015
TCCC	CCCCC	DBSM	133	0.013	61	0.007				
TCCCC	CCCCCC	DXSM	247	0.025	113	0.012				
TCC	CDCC	POSM	38	0.004	17	0.002	71	0.007	17	0.002
TCC	CCDCC	PGSM	38	0.004	17	0.002				
TCC	CCCDCC	PNSM	381	0.038	174	0.019	132	0.013	32	0.003
TCC	CCCCC	PBSM					108	0.011	27	0.003
TCCC	CCCDCC	BNSM	191	0.019	86	0.009				
TCCCC	CCCDCC	XNSM	267	0.027	121	0.013				
		Total:	1906	0.192	868	0.093	892	0.089	219	0.023
Phosphatidylserine - PS			***outer/inner ratio***		***0.00***	***1.00***			***0.00***	***1.00***
CCCC	CCCC	DPPS							46	0.005
CCCC	CDCC	POPS			200	0.021			232	0.025

CCCC	CDDC	PIPS			79	0.008			261	0.028
CCCC	CDDDC	PQPS			39	0.004				
CCCC	DDDDC	PAPS			461	0.049			326	0.034
DDDDC	DDDDC	DAPS			20	0.002				
CCCC	DDDDDC	PUPS			180	0.019			65	0.007
DDDDDC	DDDDDC	DUPS			20	0.002				
CDCC	DDDDDC	OUPS								
		Total:			999	0.107			930	0.098
Glycolipid - GM1			***outer/inner ratio***		***1.00***	***0.00***			***1.00***	***0.00***
TCC	CCCC	DPG1	89	0.009			89	0.009		
TCCC	CCCCC	DBG1					16	0.002		
TCCCC	CCCCCC	DXG1	51	0.005						
TCC	CDCC	POG1					10	0.001		
TCC	CCCDCC	PNG1	64	0.006			20	0.002		
TCCCC	CCCDCC	XNG1	51	0.005						
		Total:	255	0.026			135	0.014		
Glycolipid - GM3			***outer/inner ratio***		***1.00***	***0.00***			***1.00***	***0.00***
TCC	CCCC	DPG3	89	0.009			89	0.009		
TCCC	CCCCC	DBG3					16	0.002		
TCCCC	CCCCCC	DXG3	51	0.005						
TCC	CDCC	POG3					10	0.001		
TCC	CCCDCC	PNG3	64	0.006			20	0.002		
TCCCC	CCCDCC	XNG3	51	0.005						
		Total:	255	0.026			135	0.014		
Cerebrosides			***outer/inner ratio***						***1.00***	***0.00***
TCC	CCCC	DPGS					484	0.049		
TCCC	CCCCC	DBGS					90	0.009		
TCC	CDCC	POGS					59	0.006		
TCC	CCCDCC	PNGS					109	0.011		
		Total:					742	0.074		
Phosphatidylinositol - PI			***outer/inner ratio***		***0.00***	***1.00***			***0.00***	***1.00***
CCCC	CDCC	POPI			137	0.015			121	0.013
CCCC	CDDC	PIPI			120	0.013			48	0.005
CCCC	DDDDC	PAPI			120	0.013			121	0.013
CCCC	DDDDDC	PUPI			51	0.005			194	0.020
		Total:			428	0.046			484	0.051
Phosphatidic acid - PA			***outer/inner ratio***		***0.00***	***1.00***			***0.00***	***1.00***
CCCC	CDCC	POPA			46	0.005			13	0.001
CCCC	CDDC	PIPA			39	0.004				
CCCC	DDDDC	PAPA			39	0.004			25	0.003
CCCC	DDDDDC	PUPA			17	0.002				
		Total:			141	0.015			38	0.004
Phosphatidylinositol phosphates - PIPs			***outer/inner ratio***		***0.00***	***1.00***			***0.00***	***1.00***
CCCC	CDCC	POP1			48	0.005			15	0.002
CCCC	DDDDC	PAP1							29	0.003
CCCC	CDCC	POP2			48	0.005			15	0.002
CCCC	DDDDC	PAP2							29	0.003
CCCC	CDCC	POP3			48	0.005			15	0.002
CCCC	DDDDC	PAP3							29	0.003
		Total:			144	0.015			132	0.014
Ceramide - CER			***outer/inner ratio***		***0.65***	***0.35***			***0.50***	***0.50***

TCC	CCCC	DPCE	30	0.003	16	0.002	38	0.004	37	0.004
TCCC	CCCCC	DBCE					6	0.001	6	0.001
TCCCC	CCCCCC	DXCE	17	0.002	9	0.001				
TCC	CCCDCC	PNCE	20	0.002	12	0.001	8	0.001	8	0.001
TCC	CDCC	POCE					4	0.000	4	0.000
TCCCC	CCCDCC	XNCE	17	0.002	9	0.001				
		Total:	84	0.008	46	0.005	56	0.006	55	0.006
Lysophosphatidylcholine - LPC			***outer/inner ratio***		***1.00***	***0.00***			***0.67***	***0.33***
CCCC		PPC	64	0.006			20	0.002	10	0.001
CDCC		OPC	20	0.002						
CDDC		IPC	18	0.002			10	0.001	5	0.001
DDDDC		APC	18	0.002						
DDDDDC		UPC	7	0.001						
		Total:	127	0.013			30	0.003	15	0.002
Lysophosphatidylethanolamine – LPE			***outer/inner ratio***						***0.33***	***0.67***
CCCC		PPE					5	0.001	10	0.001
CDDC		IPE					10	0.001	20	0.002
		Total:					15	0.002	30	0.003
Diacylglycerol - DAG			***outer/inner ratio***		***0.60***	***0.40***			***0.50***	***0.50***
CCCC	CDCC	PODG	25	0.003	17	0.002	13	0.001	13	0.001
CCCC	CDDC	PIDG	23	0.002	15	0.002				
CCCC	DDDDC	PADG	23	0.002	15	0.002	25	0.003	25	0.003
CCCC	DDDDDC	PUDG	9	0.001	6	0.001				
		Total:	80	0.008	53	0.006	38	0.004	38	0.004
Cholesterol - CHOL			***outer/inner ratio***		***0.54***	***0.46***			***0.51***	***0.49***
		CHOL	3104	0.313	2656	0.285	4431	0.444	4222	0.446
Total all lipids			9913	1.000	9326	1.000	9979	1.000	9468	1.000

[a]Relative abundance of the different lipid species in the plasma membrane leaflets as well as the ratio between the leaflets. On the microsecond time scale lipids with a “proper” hydrated headgroups do not flip-flop between the leaflets and their number in each leaflet is constant. In contrast cholesterols (CHOL), ceramides (CER) and diacylglycerols (DAG) do flip-flop; therefore, their average numbers fluctuate somewhat over the simulations. The numbers reported here are initial values. Averaged over the last 10 μs of the simulations the total outer/inner leaflet counts are: CHOL 3152/2608, CER 83/47, DAG 83/50 in the **Average** and CHOL 4412/4241, CER 53/58, DAG 29/47 in the **Brain**. The Martini beads for each lipid tail are listed: C beads represent a saturated carbon chain, D beads have 1-2 cis double bonds, and T beads are below the AM1 sphingosine linker with the trans double bound. Note, the Martini O tail (representing oleic acid or palmitoleic acid) used to be CCDC but now is CDCC. The old arrangement is used in the **Average** mixture for consistency with (1).

Table S2 Lipid average order parameter[a]

			Average						Brain					
Lipid tail sn-1	Lipid tail sn-2	Acronym	Inner leaflet count	Inner tail sn-1	Inner tail sn-2	Outer leaflet count	Outer tail sn-1	Outer tail sn-2	Inner leaflet count	Inner tail sn-1	Inner tail sn-2	Outer leaflet count	Outer tail sn-1	Outer tail sn-2
Phosphatidylcholine - PC														
CCCC	CCCC	DPPC							284	0.482	0.506	531	0.536	0.553
CCCC	CDCC	POPC	550	0.475	0.440	1205	0.478	0.444	463	0.458	0.408	868	0.511	0.447
CDCC	CDCC	DOPC	49	0.417	0.434	106	0.415	0.434	118	0.371	0.395	221	0.412	0.429
CCCC	CDDC	PIPC	810	0.459	0.260	1772	0.458	0.253						
CCCC	CDDD	PFPC							32	0.459	0.183	59	0.499	0.167
CCCC	CDDCC	PEPC	32	0.463	0.283	71	0.458	0.274						
CCCC	DDDDC	PAPC	129	0.455	0.131	283	0.454	0.119	247	0.448	0.139	463	0.497	0.136
DDDDC	DDDDC	DAPC	16	0.123	0.153	35	0.108	0.137						
CCCC	DDDDDC	PUPC	32	0.455	0.112	71	0.444	0.103	90	0.456	0.076	169	0.495	0.063
CDCC	CDDC	OIPC							32	0.368	0.269	59	0.407	0.272
CDCC	DDDDDC	OUPC							22	0.370	0.075	42	0.398	0.058
Phosphatidylethanolamine - PE														
CCCC	CCDC	POPE	569	0.471	0.439	135	0.471	0.441	234	0.448	0.403	127	0.505	0.445
CDCC	CDCC	DOPE	190	0.412	0.431	44	0.415	0.434						
CCCC	CDDC	PIPE	380	0.452	0.267	90	0.454	0.261						
CCCC	CDDDC	PQPE	95	0.446	0.209	22	0.458	0.213						
CCCC	DDDDC	PAPE	522	0.449	0.130	124	0.446	0.121	574	0.442	0.136	312	0.491	0.135
DDDDC	DDDDC	DAPE	332	0.123	0.150	78	0.110	0.138						
CCCC	DDDDDC	PUPE	190	0.445	0.110	44	0.442	0.104	922	0.443	0.075	500	0.490	0.063
DDDDDC	DDDDDC	DUPE	95	0.105	0.127	22	0.091	0.117						
CDCC	CDDC	OIPE							27	0.369	0.271	14	0.401	0.277
CDCC	DDDDC	OAPE							127	0.359	0.133	68	0.394	0.132
CDCC	DDDDDC	OUPE							133	0.362	0.075	72	0.393	0.066
Sphingomyelin - SM														
TCC	CCCC	DPSM	279	0.522	0.552	611	0.529	0.564	143	0.515	0.574	581	0.565	0.611
TCCC	CCCCC	DBSM	61	0.464	0.536	133	0.470	0.545						
TCCCC	CCCCCC	DXSM	113	0.393	0.483	247	0.397	0.490						
TCC	CDCC	POSM	17	0.451	0.544	38	0.453	0.547	17	0.426	0.555	71	0.457	0.581
TCC	CCDCC	PGSM	17	0.390	0.533	38	0.404	0.557						
TCC	CCCDCC	PNSM	174	0.355	0.553	381	0.358	0.559	32	0.341	0.571	132	0.385	0.605
TCC	CCCCC	PBSM							27	0.443	0.576	108	0.497	0.610
TCCC	CCCDCC	BNSM	86	0.354	0.530	191	0.357	0.536						
TCCCC	CCCDCC	XNSM	121	0.360	0.478	267	0.363	0.483						
Phosphatidylserine - PS														
CCCC	CCCC	DPPS							46	0.488	0.507			
CCCC	CDCC	POPS	200	0.474	0.442				232	0.458	0.410			
CCCC	CDDC	PIPS	79	0.461	0.265									
CCCC	CDDDC	PQPS	39	0.462	0.214									
CCCC	DDDDC	PAPS	461	0.455	0.133				261	0.451	0.140			

DDDDC	DDDDC	DAPS	20	0.124	0.151										
CCCC	DDDDDC	PUPS	180	0.452	0.114				326	0.452	0.077				
DDDDDC	DDDDDC	DUPS	20	0.105	0.129										
CDCC	DDDDDC	OUPS							65	0.371	0.075				
Glycolipid - GM1															
TCC	CCCC	DPG1				89	0.427	0.320				89	0.488	0.494	
TCCC	CCCCC	DBG1										16	0.438	0.387	
TCCCC	CCCCCC	DXG1				51	0.340	0.361							
TCC	CDCC	POG1										10	0.385	0.567	
TCC	CCCDCC	PNG1				64	0.300	0.329				20	0.325	0.524	
TCCCC	CCCDCC	XNG1				51	0.288	0.366							
Glycolipid - GM3															
TCC	CCCC	DPG3				89	0.410	0.354				89	0.475	0.480	
TCCC	CCCCC	DBG3										16	0.428	0.473	
TCCCC	CCCCCC	DXG3				51	0.323	0.378							
TCC	CDCC	POG3										10	0.352	0.498	
TCC	CCCDCC	PNG3				64	0.294	0.345				20	0.323	0.467	
TCCCC	CCCDCC	XNG3				51	0.288	0.380							
Cerebrosides															
TCC	CCCC	DPGS										484	0.470	0.563	
TCCC	CCCCC	DBGS										90	0.433	0.533	
TCC	CDCC	POGS										59	0.363	0.549	
TCC	CCCDCC	PNGS										109	0.324	0.567	
Phosphatidylinositol - PI															
CCCC	CDCC	POPI	137	0.485	0.432				121	0.464	0.400				
CCCC	CDDC	PIPI	120	0.465	0.240				48	0.458	0.259				
CCCC	DDDDC	PAPI	120	0.454	0.098				121	0.453	0.112				
CCCC	DDDDDC	PUPI	51	0.460	0.085				194	0.454	0.047				
Phosphatidic acid - PA															
CCCC	CDCC	POPA	46	0.493	0.462				13	0.469	0.428				
CCCC	CDDC	PIPA	39	0.466	0.283										
CCCC	DDDDC	PAPA	39	0.465	0.138				25	0.458	0.147				
CCCC	DDDDDC	PUPA	17	0.460	0.120										
Phosphatidylinositol phosphates - PIPs															
CCCC	CDCC	POP1	48	0.482	0.431				15	0.463	0.404				
CCCC	DDDDC	PAP1							29	0.451	0.116				
CCCC	CDCC	POP2	48	0.487	0.436				15	0.468	0.404				
CCCC	DDDDC	PAP2							29	0.454	0.116				
CCCC	CDCC	POP3	48	0.501	0.448				15	0.475	0.410				
CCCC	DDDDC	PAP3							29	0.459	0.122				
Ceramide - CER															
TCC	CCCC	DPCE	16	0.497	0.530	30	0.497	0.530	37	0.524	0.579	38	0.524	0.579	
TCCC	CCCCC	DBCE							6	0.466	0.526	6	0.466	0.526	
TCCCC	CCCCCC	DXCE	9	0.366	0.434	17	0.366	0.434							
TCC	CCCDCC	PNCE	12	0.339	0.535	20	0.339	0.535	8	0.354	0.581	8	0.354	0.581	
TCC	CDCC	POCE							4	0.421	0.545	4	0.421	0.545	
TCCCC	CCCDCC	XNCE	9	0.335	0.427	17	0.335	0.427							
Lysophosphatidylcholine - LPC															
CCCC		PPC				64	0.520		10	0.499		20	0.549		
CDCC		OPC				20	0.451								
CDDC		IPC				18	0.279		5	0.295		10	0.304		

DDDDC		APC				18	0.150								
DDDDDC		UPC				7	0.121								
Lysophosphatidylethanolamine – LPE															
CCCC		PPE							10	0.487		5	0.544		
CDDC		IPE							20	0.289		10	0.304		
Diacylglycerol - DAG															
CCCC	CDCC	PODG	17	0.435	0.390	25	0.435	0.390	13	0.456	0.385	13	0.456	0.385	
CCCC	CDDC	PIDG	15	0.412	0.215	23	0.412	0.215							
CCCC	DDDDC	PADG	15	0.401	0.091	23	0.401	0.091	25	0.438	0.105	25	0.438	0.105	
CCCC	DDDDDC	PUDG	6	0.414	0.073	9	0.414	0.073							

[a]Lipid tail order parameters (*S*) were calculated for each lipid type as explained in the SI methods. Here we show the absolute average order parameter per tail in each leaflet. [b]DAG and CER lipids flip-flop between the leaflets, therefore, their tail order was determined jointly in both leaflets. Standard errors were calculated using block averaging; they were typically ~0.003 and all were less than 0.015, therefore, skipped for brevity. The weighted average tail order over all lipid types (excluding lipids that flip-flop) are: **Average** [0.435,0.374] / [0.430,0.301] and **Brain** [0.487,0.391] / [0.444,0.224], respectively for the [sn-1, sn-2] tails in the outer/inner leaflet.

Table S3 Lipid diffusion rates[a]

	Average						Brain					
Acronym	Outer leaflet count	Outer diffusion avg. / 10^{-7} cm^2/s	Outer diffusion error / 10^{-7} cm^2/s	Inner leaflet count	Inner diffusion avg. / 10^{-7} cm^2/s	Inner diffusion error / 10^{-7} cm^2/s	Outer leaflet count	Outer diffusion avg. / 10^{-7} cm^2/s	Outer diffusion error / 10^{-7} cm^2/s	Inner leaflet count	Inner diffusion avg. / 10^{-7} cm^2/s	Inner diffusion error / 10^{-7} cm^2/s
Phosphatidylcholine - PC												
DPPC							531	1.48	0.27	284	2.59	0.15
POPC	1205	3.41	0.24	550	4.42	0.25	868	1.76	0.07	463	2.96	0.17
DOPC	106	3.46	0.43	49	3.62	0.16	221	1.79	0.17	118	2.61	0.22
PIPC	1772	3.63	0.23	810	4.58	0.11						
PFPC							59	2.26	0.19	32	3.53	0.06
PEPC	71	2.89	0.69	32	4.31	0.96						
PAPC	283	3.21	0.11	129	5.25	0.34	463	1.98	0.17	247	2.65	0.41
DAPC	35	3.06	0.21	16	4.44	2.60						
PUPC	71	3.22	0.79	32	3.93	0.25	169	2.27	0.06	90	3.02	0.62
OIPC							59	1.81	0.01	32	2.42	0.14
OUPC							42	2.31	0.44	22	1.98	1.67
Phosphatidylethanolamine - PE												
POPE	135	2.64	0.25	569	4.05	0.02	127	1.54	0.18	234	2.31	0.02
DOPE	44	2.80	0.67	190	4.10	0.48						
PIPE	90	3.35	0.19	380	4.20	0.16						
PQPE	22	2.70	0.46	95	4.60	0.57						
PAPE	124	3.24	0.06	522	4.42	0.21	312	1.96	0.23	574	2.97	0.01
DAPE	78	3.74	0.07	332	5.02	0.03						
PUPE	44	3.83	0.68	190	4.57	0.73	500	1.88	0.11	922	2.80	0.04
DUPE	22	4.35	0.98	95	4.39	0.24						
OIPE							14	1.40	0.10	27	2.74	0.55
OAPE							68	2.39	0.01	127	2.81	0.25
OUPE							72	2.25	0.53	133	3.34	0.04
Sphingomyelin - SM												
DPSM	611	3.33	0.18	279	4.24	0.59	581	1.62	0.02	143	2.48	0.04
DBSM	133	2.33	0.54	61	4.42	0.97						
DXSM	247	2.44	0.11	113	3.62	0.17						
POSM	38	3.80	0.99	17	2.49	0.27	71	1.61	0.12	17	1.88	0.80
PGSM	38	3.81	0.60	17	6.94	2.31						
PNSM	381	2.92	0.05	174	3.81	0.09	132	1.53	0.04	32	2.19	0.35
PBSM							108	1.53	0.66	27	1.32	0.89
BNSM	191	2.83	0.08	86	4.03	0.62						
XNSM	267	2.98	0.16	121	3.73	0.03						
Phosphatidylserine - PS												
DPPS										46	2.44	0.26
POPS				200	4.47	0.12				232	2.76	0.09
PIPS				79	5.13	0.54						
PQPS				39	4.06	0.23						
PAPS				461	4.53	0.33				261	3.19	0.13

DAPS				20	3.74	0.23						
PUPS				180	4.21	0.53				326	2.98	0.06
DUPS				20	2.62	0.14						
OUPS										65	2.87	0.09
Glycolipid - GM1												
DPG1	89	1.34	0.27				89	0.74	0.05			
DBG1							16	0.49	0.19			
DXG1	51	1.10	0.20									
POG1							10	0.78	0.12			
PNG1	64	1.11	0.45				20	0.81	0.35			
XNG1	51	1.04	0.22									
Glycolipid - GM3												
DPG3	89	1.86	0.74				89	0.88	0.06			
DBG3							16	0.56	0.02			
DXG3	51	1.45	0.05									
POG3							10	0.42	0.38			
PNG3	64	2.10	0.70				20	1.20	0.46			
XNG3	51	2.04	0.85									
Cerebrosides												
DPGS							484	0.98	0.13			
DBGS							90	0.94	0.28			
POGS							59	0.79	0.35			
PNGS							109	1.06	0.01			
Phosphatidylinositol - PI												
POPI				137	4.40	0.29				121	2.59	0.08
PIPI				120	4.54	0.65				48	3.34	0.82
PAPI				120	5.08	0.28				121	2.98	0.09
PUPI				51	4.08	1.37				194	2.80	0.74
Phosphatidic acid - PA												
POPA				46	4.06	0.35				13	2.65	1.18
PIPA				39	3.93	0.39						
PAPA				39	2.97	0.51				25	1.75	1.84
PUPA				17	3.27	2.06						
Phosphatidylinositol phosphates - PIPs												
POP1				48	3.82	0.09				15	2.52	0.73
PAP1										29	2.95	0.66
POP2				48	4.26	0.31				15	2.09	0.02
PAP2										29	2.00	0.17
POP3				48	3.36	0.64				15	1.67	0.50
PAP3										29	2.56	0.29
Ceramide - CER[b]												
DPCE	30	5.78	1.47	16	5.78	1.47	38	2.35	0.16	37	2.35	0.16
DBCE							6	2.06	0.77	6	2.06	0.77
DXCE	17	4.13	0.50	9	4.13	0.50						
PNCE	20	4.44	1.24	12	4.44	1.24	8	1.69	0.35	8	1.69	0.35
POCE							4	4.63	1.15	4	4.63	1.15
XNCE	17	2.15	0.05	9	2.15	0.05						
Lysophosphatidylcholine - LPC												
PPC	64						20	1.87	0.68	10	6.67	0.46
OPC	20											
IPC	18						10	2.37	1.28	5	4.67	3.68

APC	18											
UPC	7											
Lysophosphatidylethanolamine – LPE												
PPE							5	1.29	0.17	10	2.98	0.91
IPE							10	1.64	0.77	20	4.52	0.02
Diacylglycerol - DAG[b]												
PODG	25	5.65	2.28	17	5.65	2.28	13	2.18	0.05	13	2.18	0.05
PIDG	23	6.54	1.55	15	6.54	1.55						
PADG	23	5.86	1.10	15	5.86	1.10	25	3.89	0.76	25	3.89	0.76
PUDG	9	4.05	0.06	6	4.05	0.06						
Cholesterol - CHOL[b]												
CHOL	3104	4.99	0.11	2656	4.99	0.11	4431	3.02	0.12	4222	3.02	0.12

[a]Lipid lateral diffusion was evaluated for each lipid type from the lipids' MSD in the membrane plane, see SI methods. [b]CHOL, DAG, and CER lipids flip-flop between the leaflets, therefore, their diffusion was determined jointly in both leaflets. The weighted average diffusion rates in the outer/inner leaflet (excluding lipids that flip-flop) are: **Average** 3.1±0.3 / 4.3±0.3 and **Brain** 1.6±0.2 / 2.8±0.2 in 10^{-7} cm^2/s.

Supporting References:

1. Ingólfsson, H.I., M.N. Melo, F.J. van Eerden, C. Arnarez, C.A. Lopez, T.A. Wassenaar, X. Periole, A.H. De Vries, D.P. Tieleman, and S.J. Marrink. 2014. Lipid Organization of the Plasma Membrane. J. Am. Chem. Soc. 136: 14554–14559.

2. O'Brien, J.S., and E.L. Sampson. 1965. Lipid composition of the normal human brain: gray matter, white matter, and myelin. J. Lipid Res. 6: 537–544.

3. Kishimoto, Y., B.W. Agranoff, N.S. Radin, and R.M. Burton. 1969. Comparison of the fatty acids of lipids of subcellular brain fractions. Journal of Neurochemistry. 16: 397–404.

4. Breckenridge, W.C., G. Gombos, and I.G. Morgan. 1972. The lipid composition of adult rat brain synaptosomal plasma membranes. BBA - Biomembranes. 266: 695–707.

5. Christie, W.W. 1985. Rapid separation and quantification of lipid classes by high performance liquid chromatography and mass (light-scattering) detection. J. Lipid Res. 26: 507–512.

6. Abbott, S.K., P.L. Else, T.A. Atkins, and A.J. Hulbert. 2012. Fatty acid composition of membrane bilayers: Importance of diet polyunsaturated fat balance. BBA - Biomembranes. 1818: 1309–1317.

7. Atilla-Gokcumen, G.E., E. Muro, J. Relat-Goberna, S. Sasse, A. Bedigian, M.L. Coughlin, S. Garcia-Manyes, and U.S. Eggert. 2014. Dividing Cells Regulate Their Lipid Composition and Localization. Cell. 156: 428–439.

8. Levental, K.R., J.H. Lorent, X. Lin, A.D. Skinkle, M.A. Surma, E.A. Stockenbojer, A.A. Gorfe, and I. Levental. 2016. Polyunsaturated Lipids Regulate Membrane Domain Stability by Tuning Membrane Order. Biophys. J. 110: 1800–1810.

9. Tulodziecka, K., B.B. Diaz-Rohrer, M.M. Farley, R.B. Chan, G. Di Paolo, K.R. Levental, M.N. Waxham, and I. Levental. 2016. Remodeling of the postsynaptic plasma membrane during neural development. Mol. Biol. Cell. 27: 3480–3489.

10. van Meer, G. 2005. Cellular lipidomics. EMBO J. 24: 3159–3165.

11. Fernandez, C., M. Sandin, J.L. Sampaio, P. Almgren, K. Narkiewicz, M. Hoffmann, T. Hedner, B. Wahlstrand, K. Simons, A. Shevchenko, P. James, and O. Melander. 2013. Plasma Lipid Composition and Risk of Developing Cardiovascular Disease. PLoS ONE. 8: e71846.

12. Holthuis, J.C.M., and A.K. Menon. 2014. Lipid landscapes and pipelines in membrane homeostasis. Nature. 510: 48–57.

13. Wells, M.A., and J.C. Dittmer. 1967. A comprehensive study of the postnatal changes in the concentration of the lipids of developing rat brain. Biochemistry. 6: 3169–3175.

14. Lutzke, B.S., and J.M. Braughler. 1990. An Improved Method for the Identification and Quantitation of Biological Lipids by Hplc Using Laser Light-Scattering Detection. J. Lipid Res. 31: 2127–2130.

15. Kracun, I., H. Rosner, V. Drnovsek, M. Heffer-Lauc, C. Cosović, and G. Lauc. 1991. Human brain gangliosides in development, aging and disease. Int. J. Dev. Biol. 35: 289–295.

16. Diagne, A., J. Fauvel, M. Record, H. Chap, and L. Douste-Blazy. 1984. Studies on ether phospholipids. II. Comparative composition of various tissues from human, rat and guinea pig. Biochim. Biophys. Acta. 793: 221–231.

17. Homan, R., and M.K. Anderson. 1998. Rapid separation and quantitation of combined neutral and polar lipid classes by high-performance liquid chromatography and evaporative light-scattering mass detection. J. Chromatogr. B Biomed. Sci. Appl. 708: 21–26.

18. Han, X., D.M. Holtzman, and D.W. McKeel. 2001. Plasmalogen deficiency in early Alzheimer's disease subjects and in animal models: molecular characterization using electrospray ionization mass spectrometry. J. Neurochem. 77: 1168–1180.

19. Han, X., and R.W. Gross. 2005. Shotgun lipidomics: Electrospray ionization mass spectrometric analysis and quantitation of cellular lipidomes directly from crude extracts of biological samples. Mass Spectrom. Rev. 24: 367–412.

20. Sharon, R., I. Bar-Joseph, G.E. Mirick, C.N. Serhan, and D.J. Selkoe. 2003. Altered Fatty Acid Composition of Dopaminergic Neurons Expressing -Synuclein and Human Brains with -Synucleinopathies. J. Biol. Chem. 278: 49874–49881.

21. Chan, R.B., T.G. Oliveira, E.P. Cortes, L.S. Honig, K.E. Duff, S.A. Small, M.R. Wenk, G. Shui, and G. Di Paolo. 2012. Comparative lipidomic analysis of mouse and human brain with Alzheimer disease. J. Biol. Chem. 287: 2678–2688.

22. Lam, S.M., Y. Wang, X. Duan, M.R. Wenk, R.N. Kalaria, C.P. Chen, M.K.P. Lai, and G. Shui. 2014. The brain lipidomes of subcortical ischemic vascular dementia and mixed dementia. Neurobiol. Aging. 35: 2369–2381.

23. Arai, Y., J.L. Sampaio, M. Wilsch-Bräuninger, A.W. Ettinger, C. Haffner, and W.B. Huttner. 2015. Lipidome of midbody released from neural stem and progenitor cells during mammalian cortical neurogenesis. Front. Cell. Neurosci. 9: 428–411.

24. Oliveira, T.G., R.B. Chan, F.V. Bravo, A. Miranda, R.R. Silva, B. Zhou, F. Marques, V. Pinto, J.J. Cerqueira, G. Di Paolo, and N. Sousa. 2015. The impact of chronic stress on the rat brain lipidome. Mol. Psychiatry. 21: 80–88.

25. Shevchenko, A., and K. Simons. 2010. Lipidomics: coming to grips with lipid diversity. Nat. Rev. Mol. Cell Biol. 11: 593–598.

26. Clark, J., K.E. Anderson, V. Juvin, T.S. Smith, F. Karpe, M.J.O. Wakelam, L.R. Stephens,

and P.T. Hawkins. 2011. Quantification of PtdInsP3 molecular species in cells and tissues by mass spectrometry. Nat. Meth. 8: 267–272.

27. Marrink, S.J., A.H. De Vries, and A.E. Mark. 2004. Coarse grained model for semiquantitative lipid simulations. J. Phys. Chem. B. 108: 750–760.

28. Marrink, S.J., H.J. Risselada, S. Yefimov, D.P. Tieleman, and A.H. De Vries. 2007. The MARTINI force field: coarse grained model for biomolecular simulations. J. Phys. Chem. B. 111: 7812–7824.

29. Wassenaar, T.A., H.I. Ingólfsson, R.A. Böckmann, D.P. Tieleman, and S.J. Marrink. 2015. Computational Lipidomics with insane: A Versatile Tool for Generating Custom Membranes for Molecular Simulations. J. Chem. Theory Comput. 11: 2144–2155.

30. Gu, R.-X., H.I. Ingólfsson, A.H. De Vries, S.J. Marrink, and D.P. Tieleman. 2017. Ganglioside-Lipid and Ganglioside-Protein Interactions Revealed by Coarse-Grained and Atomistic Molecular Dynamics Simulations. J. Phys. Chem. B. 121: 3262–3275.

31. Lopez, C.A., Z. Sovova, F.J. van Eerden, A.H. De Vries, and S.J. Marrink. 2013. Martini force field parameters for glycolipids. J. Chem. Theory Comput. 9: 1694–1708.

32. Pronk, S., S. Páll, R. Schulz, P. Larsson, P. Bjelkmar, R. Apostolov, M.R. Shirts, J.C. Smith, P.M. Kasson, D. van der Spoel, B. Hess, and E. Lindahl. 2013. GROMACS 4.5: a high-throughput and highly parallel open source molecular simulation toolkit. Bioinformatics. 29: 845–854.

33. de Jong, D.H., S. Baoukina, H.I. Ingólfsson, and S.J. Marrink. 2016. Martini straight: Boosting performance using a shorter cutoff and GPUs. Comput. Phys. Commun. 199: 1–7.

34. Bussi, G., D. Donadio, and M. Parrinello. 2007. Canonical sampling through velocity rescaling. J. Chem. Phys. 126: 014101.

35. Parrinello, M., and A. Rahman. 1981. Polymorphic transitions in single crystals: A new molecular dynamics method. J. Appl. Phys. 52: 7182–7190.

36. Michaud-Agrawal, N., E.J. Denning, T.B. Woolf, and O. Beckstein. 2011. MDAnalysis: A toolkit for the analysis of molecular dynamics simulations. J. Comput. Chem. 32: 2319–2327.

37. Xie, H., K.T. McDonnell, and H. Qin. 2004. Surface Reconstruction of Noisy and Defective Data Sets. Washington, DC, USA: IEEE Computer Society. pp. 259–266.

38. Kazhdan, M., M. Bolitho, and H. Hoppe. 2006. Poisson Surface Reconstruction. Aire-la-Ville, Switzerland, Switzerland: Eurographics Association. pp. 61–70.

39. Floater, M.S., and K. Hormann. 2005. Surface Parameterization: a Tutorial and Survey. In: Dodgson NA, MS Floater, MA Sabin, editors. Advances in Multiresolution for Geometric Modelling. Berlin, Heidelberg: Springer Berlin Heidelberg. pp. 157–186.

40. Venable, R.M., H.I. Ingólfsson, M.G. Lerner, B.S. Perrin, B.A. Camley, S.J. Marrink, F.L.H. Brown, and R.W. Pastor. 2017. Lipid and Peptide Diffusion in Bilayers: The Saffman-Delbrück Model and Periodic Boundary Conditions. J. Phys. Chem. B. 121: 3443–3457.

41. Castillo, N., L. Monticelli, J. Barnoud, and D.P. Tieleman. 2013. Free energy of WALP23 dimer association in DMPC, DPPC, and DOPC bilayers. Chem. Phys. Lipids. 169: 95–105.

42. Chavent, M., T. Reddy, J. Goose, A.C.E. Dahl, J.E. Stone, B. Jobard, and M.S.P. Sansom. 2014. Methodologies for the analysis of instantaneous lipid diffusion in md simulations of large membrane systems. Faraday Discuss. 169: 455–475.

43. Bremer, P.-T., G.H. Weber, V. Pascucci, M. Day, and J.B. Bell. 2010. Analyzing and tracking burning structures in lean premixed hydrogen flames. IEEE Trans. Vis. Comput. Graph. 16: 248–260.

44. Bennett, J.C., V. Krishnamoorthy, S. Liu, R.W. Grout, E.R. Hawkes, J.H. Chen, J. Shepherd, V. Pascucci, and P.-T. Bremer. 2011. Feature-based statistical analysis of combustion simulation data. IEEE Trans. Vis. Comput. Graph. 17: 1822–1831.